Contents lists available at SciOpen

Food Science and Human Wellness

journal homepage: https://www.sciopen.com/journal/2097-0765

China Food Publishing Co.

Oenothera biennis water extract inhibits the NLRP3 inflammasome by activating microglial autophagy via the AMPK-PI3K/AKT/mTOR pathway in Alzheimer's disease

Li Zhang[a,1], Lan Deng[b,1], Xiaogang Zhou[b,1], Dongsheng Fan[c], Jianming Wu[b], Chi Feng[b], Nan Jiang[b], Liwen Wei[b], Dalian Qin[b,*], Fang Ren[d,*], Lu Yu[b,*], Anguo Wu[b,e,*]

[a] *Department of Pharmacy, Neijiang Hospital of Traditional Chinese Medicine, Neijiang 641000, China*
[b] *Sichuan Key Medical Laboratory of New Drug Discovery and Drugability Evaluation, Luzhou Key Laboratory of Activity Screening and Druggability Evaluation for Chinese Materia Medica, Key Laboratory of Medical Electrophysiology of Ministry of Education, School of Pharmacy, Southwest Medical University, Luzhou 646000, China*
[c] *Department of Pharmacy, The First Affiliated Hospital of Guizhou University of Traditional Chinese Medicine, Guiyang 550005, China*
[d] *Chongqing Key Laboratory of Sichuan-Chongqing Co-construction for Diagnosis and Treatment of Infectious Diseases Integrated Traditional Chinese and Western Medicine, Chongqing Traditional Chinese Medicine Hospital, Chongqing 400021, China*
[e] *Institute of Traditional Chinese Medicine Health Industry, China Academy of Chinese Medical Sciences, Nanchang 330038, China*

ARTICLE INFO

Article history:
Received 9 October 2024
Received in revised form 6 November 2024
Accepted 19 March 2025

Keywords:
Alzheimer's disease
Oenothera biennis
NLRP3 inflammasome
Autophagy
AMPK-PI3K/AKT/mTOR
Caenorhabditis elegans
3xTg-AD mice

ABSTRACT

Alzheimer's disease (AD), an aging-related disease, is characterized by chronic neuroinflammation and microglial activation, leading to neuronal death. Targeting the NOD-like receptors family pyrin domain containing 3 (NLRP3) inflammasome may offer therapeutic benefits. Through extensive screening of a natural herbal library using lipopolysaccharide/nigericin-stimulated BV-2 microglial cells, we discovered that *Oenothera biennis*, a plant-based functional food, significantly enhanced cell survival and inhibited the NLRP3 inflammasome. This was achieved by downregulating its component proteins and suppressing pyroptosis. Similar protective effects were observed in amyloid β (Aβ) 1–42-stimulated BV-2 cells, where *O. biennis* water extract (OWE) reduced inflammasome activity and modulated microglial phagocytic function. Additionally, OWE protected neuronal PC12 cells from inflammatory damage, underscoring its neuroprotective potential. Further mechanistic studies revealed that OWE activated autophagy by regulating the AMP-activated protein kinase-phosphoinositide 3-kinase/v-akt murine thymoma viral oncogene homolog/mammalian target of rapamycin (AMPK-PI3K/AKT/mTOR) signaling pathway. The effects of OWE on NLRP3 inflammasome inhibition and pyroptosis were reversed by treatment with bafilomycin A1 and compound C, indicating that autophagy plays a key role in these processes. *In vivo* studies showed that OWE activated autophagy and ameliorated Aβ-induced paralysis and death in *Caenorhabditis elegans*. Furthermore, OWE demonstrated neuroprotective effects in 3xTg-AD mice by improving cognitive functions and reducing inflammatory markers through autophagy induction. Collectively, our findings suggest that OWE, as a plant-based functional food, inhibits the activation of the NLRP3 inflammasome in microglia via AMPK-PI3K/AKT/mTOR-mediated autophagy, providing a promising therapeutic avenue for AD.

© 2026 Beijing Academy of Food Sciences. Publishing services by Tsinghua University Press.
This is an open access article under the CC BY-NC-ND license (http://creativecommons.org/licenses/by-nc-nd/4.0/).

1. Introduction

Oenothera biennis, commonly known as evening primrose, is a plant-based functional food that has garnered attention for its medicinal properties, including treating rheumatism, strengthening muscles and bones, and alleviating conditions caused by cold and dampness. Modern pharmacological research has demonstrated that *O. biennis* possesses anti-inflammatory and antioxidant properties[1-3]. Additionally, its oil is widely recognized as a dietary supplement

[1] These authors contributed equally to this work.
* Corresponding authors.
E-mail address: dalianqin@swmu.edu.cn (D.L. Qin); renifang1993@163.com (F. Ren); yulu863@swmu.edu.cn (L. Yu); wuanguo1114@swmu.edu.cn (A.G. Wu)
Peer review under responsibility of Beijing Academy of Food Sciences.

SciOpen Publishing services by Tsinghua University Press

http://doi.org/10.26599/FSHW.2025.9250595
2213-4530/© 2026 Beijing Academy of Food Sciences. Publishing services by Tsinghua University Press. This is an open access article under the CC BY-NC-ND license (http://creativecommons.org/licenses/by-nc-nd/4.0/).

with substantial bioactivity and safety[4]. Traditionally, *O. biennis* has been utilized in herbal medicine across various cultures to treat inflammatory conditions, alleviate pain, and improve general health[5]. Recent studies further revealed its potential therapeutic applications in managing chronic inflammatory diseases and neurological disorders, owing to its rich content of bioactive compounds such as flavonoids, phenolic acids, and essential fatty acids[6]. However, the neuroprotective effects of *O. biennis* in the context of Alzheimer's disease (AD) have not been thoroughly explored.

AD, the most prevalent form of dementia, is marked by a gradual cognitive decline and distinct neuropathological traits, such as amyloid β (Aβ) plaques and neurofibrillary tangles of hyperphosphorylated tau protein[7-9]. Current therapeutic strategies primarily focus on symptomatic management, yet these treatments have limited effectiveness and do not significantly alter disease progression[10-12]. Despite extensive research, clinical trials targeting single pathological mechanisms, such as amyloid plaques, have faced repeated failures, highlighting the complexity of AD pathology and the necessity for novel approaches[13]. Consequently, therapeutic strategies addressing multiple pathological mechanisms simultaneously, particularly targeting neuroinflammation and autophagic processes, have become increasingly attractive[14-15]. In addition to these well-known characteristics, recent research has highlighted the significant role of neuroinflammation in the progression and severity of AD. Central to this inflammatory response is the NOD-like receptors family pyrin domain containing 3 (NLRP3) inflammasome, a complex protein structure within microglial cells—the brain's resident immune cells—that has been identified as a crucial contributor to AD-related inflammation[16-17].

The activation of the NLRP3 inflammasome in AD involves two primary stages: priming and activation. Priming generally occurs through the nuclear factor κB (NF-κB) pathways, which upregulate the expression of pro-inflammatory genes, including *NLRP3*[18-20]. The activation phase is triggered by various stress signals, such as mitochondrial dysfunction, lysosomal rupture, and extracellular ATP presence[17-21]. This leads to the production of active caspase-1, which processes pro-inflammatory cytokines like IL-1β and IL-18 into their active forms[22-23]. Moreover, the interaction between the NLRP3 inflammasome and amyloid plaques suggests its role in enhancing Aβ deposition and perpetuating the inflammatory milieu within the AD brain[24-25]. This exacerbates the inflammatory response and contributes to ongoing neuroinflammation, which negatively impacts neuronal health and function. Therefore, regulating NLRP3 inflammasome activity is considered a viable therapeutic strategy to mitigate inflammation-induced neuronal damage in AD[26]. Autophagy, a cellular degradation process that eliminates da maged organelles and protein aggregates[27-29], is pivotal in modulating inflammatory pathways in the brain. Recent studies indicate that enhancing autophagy in microglial cells can reduce NLRP3 inflammasome activity and its associated inflammatory response[17,30-31]. This connection underscores the potential of autophagy modulation as a therapeutic approach to control neuroinflammation in AD.

Our research specifically focused on evaluating the neuroprotective potential of natural compounds by screening various herbal extracts in lipopolysaccharide/nigericin (LPS/Nig)-treated BV-2 cells. Among these, *O. biennis* stood out for significantly enhancing cell viability. Our findings suggest that the water extract of *O. biennis* (OWE) can activate autophagy via the AMP-activated protein kinase-phosphoinositide 3-kinase/v-akt murine thymoma viral oncogene homolog/mammalian target of rapamycin (AMPK-PI3K/AKT/mTOR) pathway, potentially inhibiting NLRP3 inflammasome activation in microglial cells. This study presents a novel and promising therapeutic avenue for managing inflammation in AD, highlighting the potential of *O. biennis* as a natural product with significant neuroprotective effects. Given the urgent need for effective and safe treatments, natural products have emerged as a promising source due to their ability to target multiple pathways and their favorable safety profiles[32]. Therefore, clarifying the mechanisms by which *O. biennis* modulates neuroinflammation and autophagy could significantly advance our understanding and facilitate the development of comprehensive therapeutic strategies for AD.

2. Methods

2.1 Chemicals, plasmids, and antibodies

O. biennis was procured from the Hehuachi Medicinal Market in Chengdu, China. Acetonitrile was purchased from Adamas (Shanghai, China). The $A\beta_{1-42}$ peptide was sourced from Chinapeptides Co., Ltd. (Shanghai, China). Fetal bovine serum (FBS; #164210) was purchased from Procell, China. RPMI 1640 medium, trypsin-EDTA solution, and penicillin-streptomycin (PS) solution (100× concentration) were obtained from Gibco (Santa Clara, CA, USA). Plasmids used in this study included pEGFP-LC3 and mRFP-GFP tandem fluorescent-tagged LC3 (tfLC3), which were generously provided by Prof. Tamotsu Yoshimori from Osaka University, Japan. Additional plasmids such as pEGFP-N1-NLRP3 (PPL00151-2a), pEGFP-N1-caspase-1 (PPL00392-2e), pLVX-AcGFP1-N1-GSDMD (PPL00857-4b), and mCherry-C1-ASC (PPL01752-2b) were purchased from the Public Protein/Plasmid Library (Nanjing, China). The Lipomaster 3000 transfection reagent (TL301-02) was purchased from Vazyme (Nanjing, China). Various inhibitors and modulators were employed in the experiments, including compound C (CC; T6146), bafilomycin A1 (Baf; T6740), rapamycin (Rap; T1537), and MCC950 (T3701), all of which were obtained from TargetMol (Shanghai, China). 3-Methyladenine (3-MA; 013763227) was purchased from Adamas life (Shanghai, China), LPS was sourced from Sigma (St. Louis, MO, USA), while Nig was acquired from Selleck (Houston, TX, USA). The antibodies used in this study were as follows: mTOR (2983S), p-PI3K (4228S), PI3K (4257S), p-AMPK (2535L), and IL-1β (12426S), which were sourced from Cell Signaling Technology Inc. (Beverly, MA, USA). Additional antibodies included p-mTOR (67778-1-Ig), AMPK (66536-1-Ig), p-AKT (66444-1-Ig), AKT (60203-2-Ig), light chain 3 (LC3) (14600-1-AP), apoptosis-associated speck-like protein containing a CARD (ASC) (10500-1-AP), caspase-1 (22915-1-AP), gasdermin-D (GSDMD) (20770-1-AP), and glial fibrillary acidic protein (GFAP) (16825-1-AP), all of which were obtained from Proteintech (Wuhan, China). The antibody for NLRP3 (ab270449) was sourced from Abcam (Cambridge, MA, USA), while ionized calcium-binding adapter molecule 1 (Iba-1) (bs-1363R) and neuron-specific nuclear protein (NeuN) (bs-10394R) antibodies were obtained from Bioss (Beijing, China). All antibodies were commercially sourced, and their specificity was confirmed by the suppliers.

2.2 Preparation of *O. biennis* extract

The entire herb of *O. biennis* was initially dried and then finely ground into a powder. For the extraction process, 100 g of this powdered herb were weighed and divided into portions, each of which was soaked overnight in 800 mL of one of three different solvents: distilled water, 75% ethanol, and ethyl acetate. Each mixture was then subjected to a reflux heating process and underwent at least three repeated extraction cycles to ensure thorough extraction of the active compounds. Following the extraction cycles, the mixtures were filtered to remove solid residues. The combined filtrates from each solvent were then concentrated using a rotary evaporator to remove the solvents, resulting in three distinct extracts: OWE, the ethanol extract of *O. biennis* (OEE), and the ethyl acetate extract of *O. biennis* (OEAE). These concentrated extracts were subsequently prepared for experimental use by dissolving them in DMSO to achieve a final concentration of 100 mg/mL. Each extract was then stored appropriately until further use in the experimental procedures.

2.3 Ultra-high performance liquid chromatography system integrated with diode-array detection and quadrupole time-of-flight tandem mass spectrometry (UPLC-DAD-Q/TOF-MS/MS) conditions

To accurately analyze the chemical constituents of OWE, an UPLC-DAD-Q/TOF-MS/MS was utilized[33]. Chromatographic separation was achieved using a reversed-phase C_{18} column (2.1 mm × 100 mm, 1.7 μm; ACQUITY UPLC® BEH, Waters, USA), maintained at a constant temperature of 40 °C. The mobile phase consisted of solvent A (0.1% formic acid in water) and solvent B (acetonitrile). A gradient elution was applied as follows: 0–35 min, linear gradient from 2% to 98% B; 35–35.01 min, linear gradient returned to 2% B; 35.01–40 min, 5% B for equilibration. The flow rate was set at 0.2 mL/min, and the injection volume was 5 μL.

MS analysis was conducted using a triple TOF MS X500R system (AB SCIEX, Foster City, CA, USA) equipped with a Duo Spray source operating in negative ion mode. The electrospray ionization parameters were set as follows: electrospray voltage at –4 000 V, ion source temperature at 500 °C, and declustering potential at –50 V. Nebulizing gas pressure (GS 1) was maintained at 55 psi. Mass spectra were acquired in the *m/z* range of 100–2 000 Da, and fragmentation experiments (MS/MS) were performed using collision energy values ranging from –20 to –50 V, optimized based on precursor ions. Data analysis was performed using Analyst® software (AB SCIEX, USA). The obtained raw data were subsequently processed and analyzed with Peak View® 1.4 software. Compound identification was conducted by comparing retention times, accurate mass measurements, and fragmentation patterns with those available in relevant literature and online databases, such as METLIN and PubChem.

2.4 Cell culture

BV-2 and PC12 cell lines were obtained from the American Type Culture Collection (Rockville, MD, USA), and their authenticity was confirmed by the supplier. Additionally, stable RFP-GFP-LC3 U87 cells were provided by Dr. Xiaoming Zhu from Macau University of Science and Technology. BV-2 cells were cultured in RPMI 1640 medium, enriched with 10% FBS, 50 U/mL penicillin, and 50 μg/mL streptomycin. PC12 cells were maintained in DMEM, supplemented with 10% FBS and 1% PS. The stable RFP-GFP-LC3 U87 cells were grown in *α*-MEM supplemented with 10% FBS and 1% PS. All cell lines were cultured at 37 °C in a humidified atmosphere containing 5% CO_2, ensuring optimal growth conditions for the cells.

2.5 Cytotoxicity assay

The viability of BV-2 and PC12 cells was assessed using the 3-(4,5-dimethylthiazol-2-yl)-2,5-diphenyltetrazolium bromide (MTT; Cat. 88417; Sigma, MO, USA) assay and cell counting kit-8 (CCK-8; Cat. ST1008; Saint-Bio, Shanghai, China) assay. Cells were seeded into 96-well plates at an appropriate density and subjected to various treatments at specified time points. Following treatment, 10 μL of MTT solution (5 mg/mL) was added to each well, and the plates were incubated for 4 h at 37 °C to allow for the formation of formazan crystals. After the incubation period, the medium was carefully removed, and the formazan crystals were dissolved by adding 100 μL of DMSO to each well. The plates were then gently shaken to ensure complete dissolution of the crystals. The absorbance of the resulting solution was measured at 570 nm using a spectrophotometer. Cell viability was calculated using the following formula:

$$\text{Cell viability (\%)} = \frac{\text{Number of treated cells}}{\text{Number of control cells}} \times 100$$

The results were compiled from three independent experiments, ensuring the reliability and reproducibility of the data.

2.6 Western blot analysis

Cells or brain tissues were lysed using 1× RIPA lysis buffer (Cell Signaling Technology, Beverly, MA, USA). Protein concentrations were determined using the Bradford assay (Bio-Rad, Hercules, CA, USA). Equal amounts of protein (30–50 μg per lane) were separated by SDS-PAGE and transferred onto polyvinylidene fluoride (PVDF) membranes. The membranes were blocked with 5% non-fat milk for 1 h at room temperature to prevent nonspecific binding. After blocking, the membranes were incubated overnight at 4 °C with primary antibodies specific to the target proteins. Following the primary antibody incubation, the membranes were washed and then incubated with appropriate secondary antibodies for 1 h at room temperature. Protein bands were visualized using the supersensitive ECL kit (PD203, Oriscience, China) and detected with an automatic chemiluminescence imaging analysis system (Tanon Science & Technology Co., Ltd., Shanghai, China). The intensities of the protein bands were quantified using ImageJ software, allowing for the calculation of relative expression levels of the target proteins compared to control samples.

2.7 Hoechst/propidium iodide (PI) staining

After treatment, BV-2 and PC12 cells were fixed with 4% paraformaldehyde (PFA) for 15 min and then washed three times with PBS to remove any residual PFA. Stock solutions of Hoechst 33342 (20 mg/mL) and PI (1 mg/mL) were diluted 1:1 000 in 1 mL of RPMI 1640 complete medium to prepare the working solutions. To stain the cells, 1 μL of each working solution was added to the wells containing the fixed cells. The cells were then incubated in the dark for 30 min

to allow for sufficient staining. Following the incubation, the slides were air-dried and mounted using FluorSave™ reagent (Calbiochem, San Diego, CA, USA) to preserve fluorescence and provide a clear medium for microscopy. Fluorescence microscopy (Soptop ICX41, Ningbo, China) was utilized to capture images. The blue fluorescence from Hoechst 33342 indicated the presence of all cells, while the red fluorescence from PI indicated dead cells. Images displaying both blue and red signals were captured and combined for analysis. Cell death was quantified by calculating the percentage of cells stained with PI relative to those stained with Hoechst 33342, providing an accurate assessment of cell viability post-treatment. This calculation was performed by counting the number of PI-positive cells (red) and dividing by the total number of Hoechst-positive cells (blue), with results expressed as a percentage.

2.8 YO-PRO-1/Eth-D2 staining

The detection of apoptotic and pyroptotic BV-2 cells was performed using YO-PRO-1/Eth-D2 staining[34]. Working solutions were prepared by diluting 1 μL each of YO-PRO-1 (1 mmol/L, Beyotime, C2022-1 mL), Eth-D2 (2 mmol/L), and Hoechst 33342 in 1 mL of RPMI 1640 complete medium to achieve a 1:1 000 dilution. Following the treatment of cells, the prepared staining solutions were added to the wells, and the cells were incubated in the dark for 30 min. After incubation, the cells were washed twice with PBS to remove any excess stain. The slides were then air-dried and mounted using FluorSave™ reagent (Calbiochem, San Diego, CA, USA) to preserve fluorescence. Fluorescence microscopy was utilized to capture images displaying green, red, and blue signals. YO-PRO-1 (green) stains apoptotic cells, Eth-D2 (red) stains pyroptotic cells, and Hoechst 33342 (blue) stains all nuclei. The images were captured and merged to show the different states of the cells. Apoptotic and pyroptotic cells were identified based on the distinct staining patterns: cells that stained with YO-PRO-1 indicated apoptosis, while those stained with Eth-D2 indicated pyroptosis. The merged images allowed for the comprehensive visualization and differentiation of the apoptotic and pyroptotic cells within the BV-2 cell population.

2.9 Caspase-3 activity assay

To assess caspase-3 activity in PC12 cells, the GreenNuc™ caspase-3 assay kit for live cells (Beyotime, Cat. C1168M) was employed[35]. Following the treatment with the conditioned medium, PC12 cells were prepared for the assay according to the manufacturer's instructions. Briefly, cells were washed with PBS to remove any residual medium. Subsequently, the cells were incubated with the caspase-3-specific fluorogenic substrate (FLICA) reagent and Hoechst 33342 for 1 h at 37 °C. The FLICA reagent binds to active caspase-3, allowing for fluorescent detection. After incubation, the cells were washed again with the provided wash buffer to remove any excess probe, ensuring specific and accurate detection of caspase-3 activity. Fluorescence microscopy was used to capture images of the stained cells. The fluorescence intensity, indicative of caspase-3 activity, was quantified using ImageJ analysis software. To ensure representative data, at least five fields per sample were analyzed. This comprehensive analysis allowed for a precise assessment of caspase-3 activity in the PC12 cells post-treatment.

2.10 Determination of phagocytosis in BV-2 microglial cells

2.10.1 Preparation of $A\beta_{1–42}$

$A\beta_{1–42}$ peptide was prepared following previously established methods[31]. Initially, lyophilized $A\beta_{1–42}$ peptide was monomerized by dissolving it in hexafluoroisopropanol (HFIP) to achieve a concentration of 1 mmol/L. The solution was then aliquoted into sterile microcentrifuge tubes. The HFIP was subsequently evaporated under vacuum, resulting in a dry peptide film. This peptide film was stored in a desiccated state at –20 °C until needed for further experiments. This method ensures that the $A\beta_{1–42}$ peptide is in a monomeric form, suitable for use in experimental procedures.

2.10.2 Preparation of pH-sensitive fluorescent human Aβ conjugate ($A\beta^{pH}$)

To facilitate the study of BV-2 cell phagocytosis, $A\beta^{pH}$ was prepared as described previously[36]. Initially, 200 μL of $A\beta_{1–42}$ (1 mg/mL, dissolved in 1 mol/L $NaHCO_3$, pH ~8.3) was mixed with 10 equivalents of Protonex™ Green 500 SE dye (88 μL from a 5 mmol/L stock in anhydrous DMSO). The mixture was incubated in the dark at room temperature for 3 h, followed by the addition of 5 equivalents of the dye (44 μL) and further incubation under the same conditions for an additional 3 h. Subsequently, the mixture was diluted with 1 mL of ultrapure water and centrifuged at 4 500 × *g* for 30–45 min using a protein concentrator with a 3 kDa molecular weight cut-off (Thermo Fisher Scientific, Cat. #PI88514) to remove low molecular weight fragments. The concentrated solution was then diluted with 0.5 mL of ultrapure water, dialyzed for 30 min, and finally diluted with 0.2 mL of ultrapure water before being lyophilized overnight to yield $A\beta^{pH}$ powder for subsequent use.

2.10.3 Real-time phagocytosis assay

To monitor phagocytosis in BV-2 microglial cells, $A\beta^{pH}$ fluorescent probes were used with the IncuCyte® Live-Cell Analysis System (Essen BioScience, Ann Arbor, MI, USA)[37]. BV-2 cells were cultured in 96-well plates at 37 °C and 5% CO_2. The $A\beta^{pH}$ probes were prepared by reconstituting the lyophilized material in PBS, vortexing the solution, and incubating it at 37 °C for 30 min. The probes were then centrifuged and washed twice with PBS before being resuspended in RPMI-1640 supplemented with 10% FBS. The resuspended probes were added to the BV-2 cells, which had been pre-treated with or without OWE, just prior to imaging. The plate was then installed in the IncuCyte® system, which was configured to capture images at 3-min intervals for the first 3 h and then at hourly intervals for a total duration of 24 h, using a 10× objective in a temperature-controlled incubator. Phagocytic activity was analyzed by quantifying the intensity of red fluorescence using the IncuCyte S3 2019B software. This provided a measure of the extent to which BV-2 cells internalized the $A\beta^{pH}$ probes. Additionally, video recordings of the real-time phagocytosis process were made available for detailed temporal analysis, offering insights into the dynamics and efficiency of phagocytosis over the 24-h period.

2.11 Transmission electron microscopy (TEM)

BV-2 cells were treated with OWE (40 μg/mL), Rap (10 μmol/L), or left untreated as a control for the indicated durations. After treatment, cells were collected and fixed with 2.5% glutaraldehyde at 4 °C overnight. Samples were subsequently washed with PBS and post-fixed in 1% osmium tetroxide for 1 h at 4 °C. After dehydration in an ascending ethanol gradient (50%, 70%, 90%, 100%), samples were embedded in epoxy resin. Ultrathin sections (60–80 nm) were cut using an ultramicrotome, stained with uranyl acetate and lead citrate, and observed under a TEM (Zeiss, Germany) to analyze autophagic structures and autophagosomes formation. Representative images were captured to evaluate autophagy-related morphological changes.

2.12 Caenorhabditis elegans maintenance

The *C. elegans* strains DA2123 (adIs2122 [*lgg-1p*::GFP::Lgg-1+ *rol-6*(su1006)]) were obtained from the Department of Physiology, School of Medicine, Tokyo Women's Medical University, Tokyo, Japan. Wild type N2, BC12921 (sIs10729 [rCes T12G3.1::GFP+pCeh361]), CL2331 (dvIs37 [*myo-3p*::GFP::A*β*(3–42)+*rol-6*(su1006)]) and CL4176 (pAF29 [*myo-3p*::Aβ(1–42)+(p RF4)*rol-6*(su1006)]) were all sourced from the Caenorhabditis Genetics Center, University of Minnesota, Minneapolis, MN, USA. Unless otherwise noted, all strains were maintained on nematode growth medium (NGM) plates at 20 °C and fed with *E. coli* OP50. This standardized maintenance ensured the health and consistency of the worm populations used in the experiments.

2.13 Autophagy detection in C. elegans

To assess autophagic activity in *C. elegans*, the BC12921 and DA2123 strains were utilized[38]. For the BC12921 strain, worms were seeded into 96-well plates containing 100 μL of M9 buffer and pretreated with or without OWE or Rap for 7 days. After the treatment period, representative images were captured using a fluorescence microscope (Leica DM6B, Leica Microsystems GmbH, Germany) equipped with a 10× objective lens and appropriate filters (excitation wavelength at 488 nm and emission wavelength at 520 nm). At least 15 worms per condition. The fluorescence intensity of p62 within the worms was measured using ImageJ software (version 1.53, NIH, Bethesda, MD, USA), applying identical threshold settings across all groups to ensure consistency and reproducibility. For the DA2123 strain, autophagic activity was monitored by counting GFP::LGG-1 fluorescent puncta. Worms were treated with or without OWE or Rap for 48 h, after which they were placed on 2% agarose pads containing 0.1% NaN_3 to immobilize them. GFP::LGG-1 puncta were then imaged under the same fluorescence microscope with a 20× objective lens, excitation at 488 nm and emission at 520 nm. Imaging parameters (exposure time, gain, and intensity) were uniformly maintained for all groups to facilitate direct comparison. The number of GFP::LGG-1 puncta per worm was quantified in equivalent-sized regions across all experimental conditions using ImageJ software, At least 10–20 worms per group were analyzed, and GFP puncta were manually counted by two independent observers blinded to experimental conditions to ensure unbiased and reproducible quantification.

2.14 Determination of $A\beta_{3-42}$ aggregation

The aggregation of $A\beta_{3-42}$ in the CL2331 strain, which expresses thermosensitive human GFP-$A\beta_{3-42}$ in body wall muscles, was analyzed[7]. Worms were treated with or without OWE and cultured at 25 °C to induce $A\beta_{3-42}$ aggregation until day 2. Subsequently, worms were transferred to microscope slides containing 0.1% NaN_3. Representative images were captured with a fluorescence microscope (Leica DM6B, Leica Microsystems GmbH, Germany), and the aggregation of $A\beta_{3-42}$ was quantified across the whole worm area.

2.15 Paralysis assay in CL4176 strain

The paralysis assay using the *C. elegans* CL4176 strain, a model organism for studying Aβ-induced toxicity, was conducted according to established protocols[7]. In brief, synchronized young adult nematodes were grown at a permissive temperature of 16 °C. Upon reaching the onset of adulthood, the temperature was shifted to 25 °C to induce the expression of Aβ. The nematodes were observed at regular intervals, typically every 2–4 h, following the temperature shift. Paralysis was assessed by gently prodding the worms with a platinum wire. A worm was scored as paralyzed if it failed to move its body in response to the stimulus, with only minimal movement of the head or tail being allowed. For statistical analysis, at least 150 worms were included in each experimental group. The data collected from these observations provided insights into the impact of treatments on Aβ-induced paralysis in the CL4176 strain, thereby contributing to the understanding of potential therapeutic effects of tested compounds.

2.16 RNA interference (RNAi)

RNAi was utilized to silence specific genes in CL4176 worms[38]. Gene knockdown in the nematodes was achieved by feeding them bacteria engineered to produce RNA targeting the genes of interest, following previously described methods. In this process, the HT115 strain of *E. coli* was grown overnight in LB medium supplemented with 50 μg/mL ampicillin at 37 °C. To induce the production of double-stranded RNA, 5 mmol/L isopropyl *β-D*-1-thiogalactopyranoside was added to the bacterial cultures. Subsequently, L1 stage worms, pre-treated with or without OWE, were exposed to the bacteria expressing RNAi targeting the autophagy-related gene *lgg-1*. This RNAi treatment enabled the specific silencing of *lgg-1*, allowing for the assessment of its role in autophagy and the overall impact on Aβ-induced toxicity in the CL4176 strain. The effectiveness of gene knockdown and subsequent phenotypic changes were monitored and analyzed to elucidate the potential therapeutic effects of OWE on autophagy modulation in this model system.

2.17 Lifespan analysis

To analyze the lifespan of PA14-treated N2 worms with or without OWE, a standardized protocol was followed[39]. Synchronized L4 stage N2 worms were exposed to the PA14 pathogen by transferring them onto NGM plates seeded with a lawn of PA14 in

the presence or absence of OWE. The worms were maintained at 20 °C throughout the experiment. Lifespan scoring commenced 24 h after exposure to PA14. Worms were observed daily, and those that failed to respond to gentle prodding with a platinum wire were recorded as dead and removed from the plates. Worms that crawled off the plate, displayed internal hatching, or exhibited vulva bursting were censored from the analysis. To prevent the growth of progeny, worms were transferred to fresh PA14-seeded plates every other day during the reproductive period. Data were compiled from three independent experiments, each with at least 50 worms per condition. The lifespan data were analyzed using Kaplan-Meier survival curves and log-rank (Mantel-Cox) tests to determine statistical significance between different treatment groups.

2.18 Uranine staining in C. elegans

To evaluate cell death in the intestines of CL4176 worms, uranine staining was employed[40]. The procedure began by preparing the uranine staining solution by dissolving uranine in M9 buffer to a final concentration of 10 μg/mL. After treatment, CL4176 worms were washed three times with M9 buffer to remove any residual debris and subsequently incubated in the uranine staining solution for 1 h at room temperature in the dark. Post-incubation, the worms were washed more than three times with M9 buffer to eliminate excess dye. The stained worms were then mounted on agar pads and anesthetized with a drop of 10 mmol/L NaN_3. Using fluorescence microscopy, images of the intestines were captured, visualizing uranine staining with a GFP filter. The images were analyzed to assess cell viability, with bright green fluorescence indicating viable cells.

2.19 Acridine orange staining in C. elegans

To evaluate cell death in the intestines of CL4176 worms, acridine orange staining was employed[40]. The procedure began with the preparation of the staining solution by dissolving acridine orange (Cat. IA8080, Solarbio, Beijing, China) in M9 buffer to achieve a final concentration of 10 μg/mL. After treatment, CL4176 worms were washed three times with M9 buffer to remove any residual bacteria and then incubated in the acridine orange staining solution for 30 min at room temperature in the dark. Following incubation, the worms were washed three times with M9 buffer to remove excess dye. For microscopy and analysis, the stained worms were mounted on agar pads and anesthetized with a drop of 10 mmol/L NaN_3. Fluorescence microscopy was used to capture images of the intestines of the stained worms, visualizing acridine orange staining with a TRITC filter. The images were analyzed to assess cell death, with orange/red fluorescence indicating dead or dying cells.

2.20 4',6-Diamidino-2-phenylindole (DAPI) staining in C. elegans

To assess cell death in *C. elegans*, DAPI staining was utilized[40]. Synchronized young adult N2 worms were washed three times with M9 buffer to remove any residual debris. The worms were then fixed in 4% PFA for 30 min at room temperature. After fixation, the worms were washed three times with M9 buffer and permeabilized with 0.1% Triton X-100 in PBS for 20 min. Following permeabilization, the worms were incubated in a DAPI staining solution (1 μg/mL in PBS) for 30 min in the dark at room temperature. Excess stain was removed by washing the worms three times with M9 buffer. The stained worms were mounted on agar pads and anesthetized with a drop of 10 mmol/L NaN_3. Using fluorescence microscopy, images were captured to visualize DAPI staining, which binds to DNA and indicates cell nuclei. Healthy cells exhibit uniform, round nuclei with bright fluorescence, while apoptotic or necrotic cells display fragmented or condensed nuclei. The extent of cell death was quantified by counting the number of abnormal nuclei in the intestinal region using ImageJ software.

2.21 Animals and drug administrations

All animal care and experimental procedures were conducted under the approval of the Animal Care and Use Committee of Southwest Medical University (approval No. 20240514-002). We utilized two strains of mice: 3xTg-AD mice (#034830-JAX) sourced from the Jackson Laboratory, and B6;129 mice obtained from Vital River, Beijing, China. Both strains were housed together under specific pathogen-free conditions with controlled environmental parameters (relative humidity of 40%–60%, a temperature range of 20–24 °C, and a 12-h/12-h light/dark cycle) in our laboratory facility. Seven-month-old mice (half male and half female) weighing between 22 and 28 g were randomly assigned to four groups, each consisting of eight mice (4 males and 4 females per group): a control group (normal B6;129 mice), a model group (3xTg-AD mice), a low-dose treatment group (3xTg-AD mice, 50 mg/kg), and a high-dose treatment group (3xTg-AD mice, 100 mg/kg)[6,41]. The treatment groups received daily intraperitoneal injections of OWE at a fixed time of 6 p.m. over 40 days. The control and model groups were administered an equivalent volume of 0.9% saline. Post-treatment, the cognitive functions of the mice were evaluated. Following the behavioral assessments, all mice were euthanized, and their brains were harvested for further analysis. The brains from four mice per group were fixed in 4% PFA for subsequent immunohistochemistry and immunofluorescence staining, whereas the brains from the remaining four mice per group were preserved at –80 °C for Western blot analysis.

2.22 Morris water maze (MWM) test

The MWM test was employed to evaluate the behavioral cognitive functions of mice following treatment with OWE[30]. The test involved a large circular pool filled with opaque water, which was segmented into four quadrants. A platform was submerged just below the water surface in one of these quadrants, serving as the goal for the mice. During the training phase, mice were released from various starting positions around the perimeter of the pool, with the task of locating the hidden platform. To prevent learning biases, the starting positions were randomized for each trial. Each trial continued until the mice found the platform or a maximum of 60 s elapsed. Mice that were unable to locate the platform within this timeframe were gently guided to it. This phase was repeated over several days to allow the mice to learn the location of the platform. After the training phase, a probe trial was conducted to evaluate the mice's memory retention. In this trial, the platform was removed, and the mice were placed in the pool from a new starting position. Their recall of the platform's previous location was assessed by recording the time spent in the quadrant

where the platform was originally located. Data collection, including path efficiency and swim speed, was facilitated by overhead cameras connected to specialized software, ensuring precise measurement of the cognitive functions of the mice.

2.23 Immunofluorescence assay

To evaluate protein expression and localization in cells or tissue sections, an immunofluorescence assay was performed[31]. Cells or tissue sections were first fixed in 4% PFA for 15 min at room temperature. After fixation, the samples were washed three times with PBS and then permeabilized with 0.1% Triton X-100 in PBS for 10 min. Following permeabilization, the samples were blocked with 5% bovine serum albumin in PBS for 1 h at room temperature to prevent non-specific binding. Primary antibodies specific to the target proteins were then applied, and the samples were incubated overnight at 4 °C. After incubation, the samples were washed three times with PBS to remove unbound primary antibodies. Next, fluorophore-conjugated secondary antibodies were applied, and the samples were incubated for 1 h at room temperature in the dark. Following secondary antibody incubation, the samples were washed three more times with PBS. For nuclear staining, DAPI was added at a concentration of 1 μg/mL for 5 min, followed by a final wash with PBS. The samples were then mounted on slides using an antifade mounting medium. Images were captured using a fluorescence microscope, and the localization and intensity of fluorescence were analyzed to determine the expression levels and distribution of the target proteins.

2.24 Statistical analysis

All statistical analyses were conducted using data from at least three independent experiments. Results are expressed as the mean ± standard deviation (SD). Statistical analyses were performed using GraphPad Prism version 8.0. A one-way analysis of variance followed by Tukey's post-hoc test was used to assess differences among various groups. Differences were considered statistically significant at a *P*-value of less than 0.05.

3. Results

3.1 OWE inhibits cell death in LPS/Nig-stimulated BV-2 cells

Our study aimed to identify potential inhibitors of NLRP3 inflammasome activation, a critical factor in triggering pyroptosis. Using an *in vitro* model of BV-2 microglial cells activated by LPS/Nig, we screened a library of herbal extracts. Out of 288 extracts, OEE was found to be the most effective, significantly enhancing cell viability (Figs. 1A and B). To further investigate the bioactive constituents in OEE, we extracted *O. biennis* using various solvents, such as ethyl acetate and water, to differentiate between their lipophilic and hydrophilic properties. The cytotoxicity of these extracts was initially evaluated in BV-2 cells using an MTT assay (Figs. 1C–E). Subsequent treatments with non-toxic doses and MCC950 (an inhibitor with selectivity for NLRP3) were then applied to LPS/Nig-stimulated BV-2 cells. As shown in Figs. 1F–G, LPS/Nig-stimulated BV-2 cells exhibited significant PI staining, indicating cell death, and displayed morphological changes characteristic of pyroptosis. In contrast, treatments with OEAE, OEE, and especially OWE notably reduced cell death and mitigated morphological damage caused by LPS/Nig. Additionally, OWE showed the greatest efficacy in restoring cell viability in LPS/Nig-stimulated BV-2 cells (Fig. 1H). Preliminary chemical profiling of OWE was carried out using UPLC-DAD-TOF-MS/MS. The detailed chromatograms (Fig. 1I) and the list of components identified (Table S1) revealed compounds such as ellagic acid, gallic acid, quercetin, and oenothein B, which may contribute to the effect of OWE on inhibiting cell death in LPS/Nig-stimulated BV-2 cells.

3.2 OWE inhibits the activation of NLRP3 inflammasome and pyroptosis in LPS/Nig-stimulated BV-2 cells

The NLRP3 inflammasome plays a pivotal role in regulating pyroptosis and inflammatory responses in microglial cells, which are crucial for the cellular mechanisms underlying neuroinflammation and related pathologies[42]. To elucidate the potential therapeutic effects of OWE, we investigated its impact on the activation of the NLRP3 inflammasome in LPS/Nig-stimulated BV-2 cells. Our initial experiments employed Western blot analysis to assess the protein levels of NLRP3 inflammasome components, including NLRP3, ASC, caspase-1, GSDMD, and IL-1β, in LPS/Nig-stimulated BV-2 cells. As depicted in Figs. 2A–F, OWE significantly reduced the expression of NLRP3 and ASC, as well as the levels of cleaved caspase-1, N-GSDMD, and cleaved-IL-1β. Furthermore, transient transfection of BV-2 cells with pEGFP-N1-NLRP3, pEGFP-N1-caspase-1, or pmCherry-C1-ASC, followed by fluorescence microscopy, revealed a decrease in GFP and mCherry fluorescence intensity upon treatment with OWE (Figs. 2G–J). These data suggest that OWE effectively inhibits the activation of the NLRP3 inflammasome. Additionally, using Hoechst/PI staining to assess cell death, we observed a significant reduction in PI-positive cells in the presence of OWE, indicating its protective effect against LPS/Nig-induced pyroptosis (Figs. 2K and L). To further explore the effect of OWE on pyroptosis inhibition, we employed YO-PRO-1/Eth-D2 staining to detect the formation of GSDMD pores on the cell membrane. Figs. 2M and N demonstrate that OWE markedly diminished the number of YO-PRO-1 positive cells, indicating a significant inhibition of GSDMD pore formation. After treatment with Triton X-100, all cells stained positively with YO-PRO-1 and Eth-D2, confirming the disruption of cell membrane integrity. Moreover, immunofluorescence assays further corroborated these findings, showing a significant reduction in GSDMD expression at the cell membrane in OWE-treated cells compared to those stimulated with LPS/Nig alone (Fig. 2O). This suggests that OWE not only prevents the assembly of the NLRP3 inflammasome but also blocks the execution phase of pyroptosis by inhibiting GSDMD pore formation. Collectively, OWE acts as a potent inhibitor of NLRP3 inflammasome activation and pyroptosis, offering a promising therapeutic strategy for conditions characterized by excessive inflammatory responses and cell death.

3.3 OWE inhibits the activation of NLRP3 inflammasome and cell phagocytosis in $A\beta_{1-42}$-stimulated BV-2 cells

In the context of AD, activation of the NLRP3 inflammasome within microglial cells has been linked to inflammatory processes

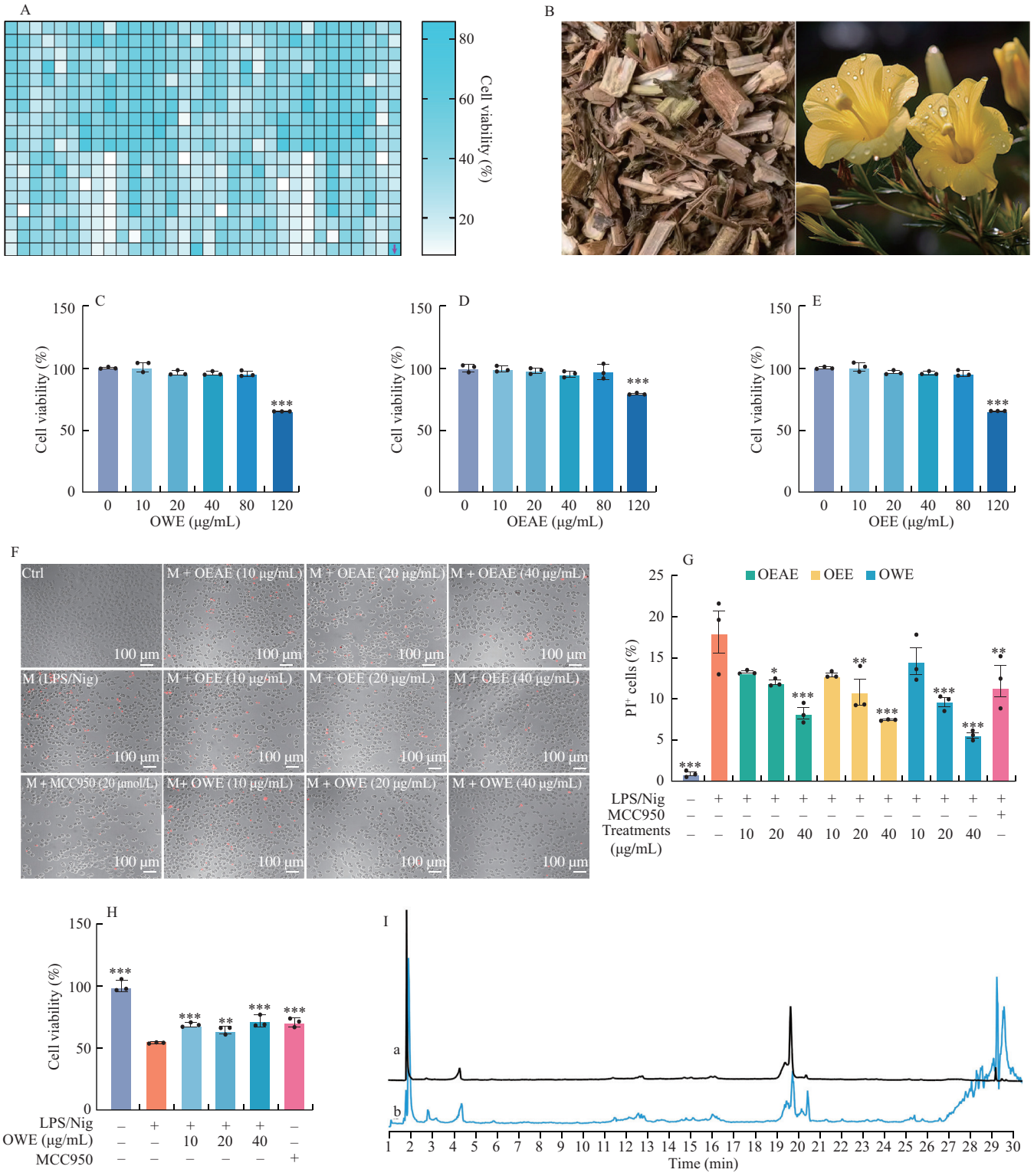


Fig. 1 OWE inhibits cell death in LPS/Nig-stimulated BV-2 cells. (A) Screening of active herbal extracts effectively inhibiting the cell death of LPS/Nig-stimulated BV-2 cells. OEE was highlighted by a red arrow. (B) Photos displaying the medicinal material and plant morphology of *O. biennis*. (C–E) Viability of BV-2 cells treated with OWE, OEAE, and OEE at specified concentrations. ***$P < 0.001$ *vs*. control group. (F) Representative images of merged white light and PI-stained BV-2 cells stimulated with LPS/Nig in the presence or absence of OWE, OEAE, and OEE at indicated concentrations. Magnification 20×, scale bar 100 μm. (G) Percentage of cells exhibiting PI signals. (H) Cell viability of LPS/Nig-stimulated BV-2 cells treated with OWE at various concentrations. (I) Representative (a) HPLC-DAD chromatogram and (b) total ion chromatogram of OWE. Data are expressed as mean ± SD. *$P < 0.05$, **$P < 0.01$, ***$P < 0.001$ *vs*. LPS/Nig positive control group.

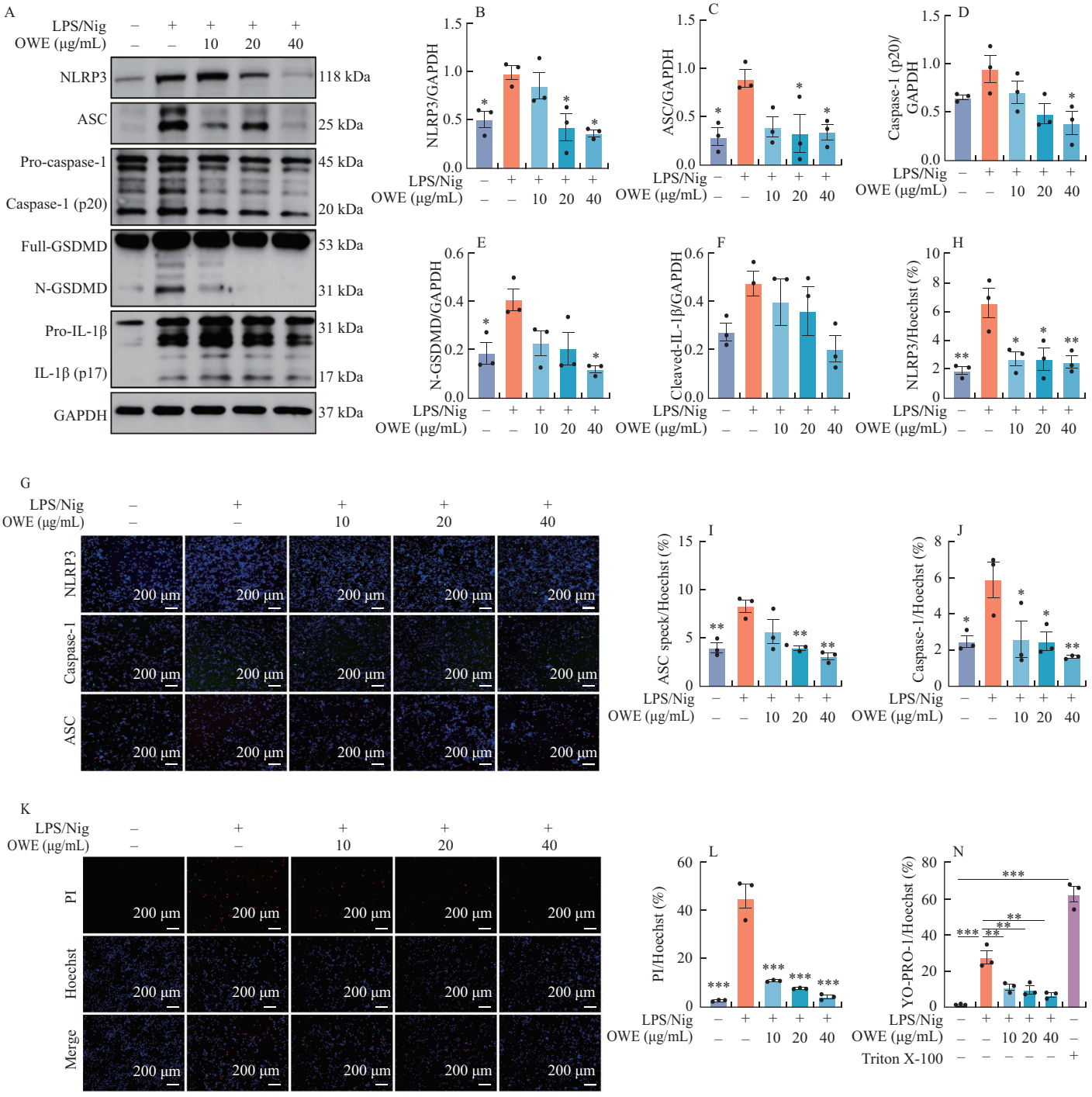


Fig. 2 OWE inhibits the activation of NLRP3 inflammasome and pyroptosis in LPS/Nig-stimulated BV-2 cells. (A) Representative Western blot images showing NLRP3, ASC, caspase-1, GSDMD, IL-1β, and GAPDH in BV-2 cells stimulated with LPS/Nig and treated with OWE at specified concentrations. Original and non-processed Western blot images are available in Fig. S1. (B–F) Relative protein expressions of NLRP3, ASC, caspase-1 (p20), N-GSDMD, and cleaved-IL-1β to GAPDH, respectively. (G) Representative images of BV-2 cells transiently transfected with pEGFP-N1-NLRP3, pEGFP-N1-caspase-1, or pmCherry-C1-ASC and Hoechst-stained, stimulated with LPS/Nig in the presence or absence of OWE at indicated concentrations. Magnification 10×, scale bar 200 μm. (H–J) Relative percentages of NLRP3, ASC, and caspase-1 to Hoechst. (K) Representative images of Hoechst/PI-stained BV-2 cells stimulated with LPS/Nig in the presence or absence of OWE. Magnification 10×, scale bar 200 μm. (L) The ratio of PI to Hoechst in BV-2 cells. (M) Representative images of YO-PRO-1/Eth-D2-stained BV-2 cells stimulated with LPS/Nig in the presence or absence of Triton X-100 and OWE. Magnification 10×, scale bar 200 μm. (N) The ratio of YO-PRO-1 to Hoechst in BV-2 cells. (O) Representative confocal images demonstrating the immunofluorescence expression of GSDMD in Hoechst-stained BV-2 cells stimulated with LPS/Nig in the presence or absence of 40 μg/mL OWE. Magnification 63×, scale bar 10 μm. Data are expressed as mean ± SD. *$P < 0.05$, **$P < 0.01$, ***$P < 0.001$ *vs*. LPS/Nig positive control group.

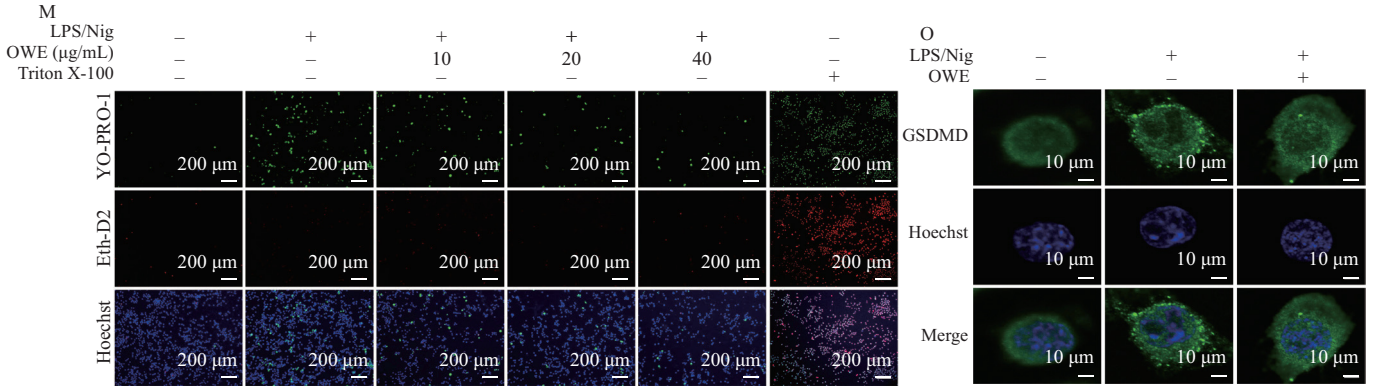


Fig. 2 (*Continued*)

that exacerbate disease pathology[17]. To simulate the pathological environment of AD, we stimulated BV-2 microglial cells with $A\beta_{1-42}$, known to trigger NLRP3 inflammasome activation and subsequent pyroptosis. Initially, transient transfection of BV-2 cells with pEGFP-N1-NLRP3, pEGFP-N1-caspase-1, or pmCherry-C1-ASC, followed by fluorescence microscopy assessment, showed that OWE substantially reduced the fluorescence intensity of GFP and mCherry, indicating a suppression of NLRP3 inflammasome assembly (Figs. 3A–D). This was corroborated by Western blot analyses, which revealed significant decreases in the levels of cleaved caspase-1 and mature IL-1β in cells treated with OWE (Figs. 3E–G). These findings confirm that OWE effectively inhibits the activation of the NLRP3 inflammasome triggered by $A\beta_{1-42}$. Given that microglial phagocytic activity is crucial for the clearance of Aβ plaques but can become dysregulated under inflammatory conditions[34], we used the IncuCyte® Live-Cell Analysis System to monitor the phagocytic activity of BV-2 cells after stimulation with $A\beta_{1-42}$. Our results illustrated that while $A\beta_{1-42}$ markedly enhanced phagocytic activity within 30 min, this response plateaued shortly thereafter. In contrast, treatment with OWE significantly attenuated the Aβ-induced enhancement of phagocytic activity (Figs. 3H–J and Videos S1 and 2 in Supplementary Material). This suggests that OWE not only protects microglial cells from overactivation but also helps normalize their functional response following exposure to Aβ. In summary, our data indicate that OWE can both inhibit the pathological activation of the NLRP3 inflammasome and modulate microglial phagocytic function in Aβ-stimulated BV-2 cells.

3.4 OWE decreases the conditioned medium-induced death in PC-12 cells

Studies have shown that inflammatory cytokines secreted by overactivated microglial cells can exacerbate neuronal death, a key feature in AD[43]. To investigate the potential neuroprotective effects of OWE, we explored its impact on neuronal viability under conditions of microglia-induced inflammation. Initially, we assessed the cytotoxicity of OWE alone and in combination with LPS/Nig on PC12 cells. The results indicated that neither OWE alone nor its combination with LPS/Nig exhibited significant cytotoxic effects (Figs. 4A and B). Subsequently, conditioned media were collected from BV-2 microglial cells treated with LPS/Nig in the presence or absence of OWE. These conditioned media were then applied to PC12 cells to evaluate the effects on neuronal viability, death, and apoptosis using the MTT assay, Hoechst/PI staining, and caspase-3 staining analysis (Fig. 4C). The results showed that conditioned media from LPS/Nig-treated BV-2 cells significantly reduced the viability and increased the death of PC12 cells. However, when OWE was included in the BV-2 cell treatment, the conditioned media significantly enhanced cell viability and decreased cell death in PC12 cells (Figs. 4D–F). Furthermore, fluorescence expression of caspase-3, a key executor of apoptosis, was markedly reduced in PC12 cells treated with conditioned media from OWE-modulated BV-2 cells (Figs. 4G and H), suggesting that OWE effectively mitigates the apoptosis induced by inflammatory cytokines in PC12 cells. Overall, our results demonstrate that OWE protects PC12 cells from inflammatory damage induced by microglia, highlighting its therapeutic potential for inflammation-related neuronal injuries in AD.

3.5 OWE activates autophagy by regulating the AMPK-PI3K/AKT/mTOR signaling pathway

Autophagy, a cellular process critical for removing damaged organelles and proteins, has been shown to inhibit the activity of the NLRP3 inflammasome[44]. To investigate the potential of OWE to induce autophagy, we conducted a series of experiments focusing on its effects in BV-2 microglial cells and stable GFP-RFP-LC3 U87 cells. Our initial experiments examined the activation of autophagy in response to various concentrations of OWE, OEAE, and OEE in stable GFP-RFP-LC3 U87 cells. Figs. 5A and B reveal that all extracts significantly increased the number of GFP-LC3 puncta within the cells, with OWE showing the most pronounced effect at equivalent concentrations. Furthermore, Western blot analysis assessed the impact of OWE on LC3 protein expression in BV-2 cells. As shown in Figs. 5C and D, OWE notably increased the ratio of LC3-II to LC3-I, indicating enhanced autophagosome formation. To further investigate the effect of OWE on autophagic flux, we utilized the autophagy inhibitors 3-MA and Baf. The results showed that 3-MA significantly inhibited the formation of GFP-LC3 puncta induced by OWE in U87 cells, while Baf further increased their formations (Figs. 5E and F). Moreover, the effects of OWE on RFP-LC3 and GFP-LC3 puncta formation were assessed under the influence of Baf. As indicated in Figs. 5G and H, OWE and the known autophagy inducer Rap significantly decreased the GFP/RFP ratio, indicating an increase

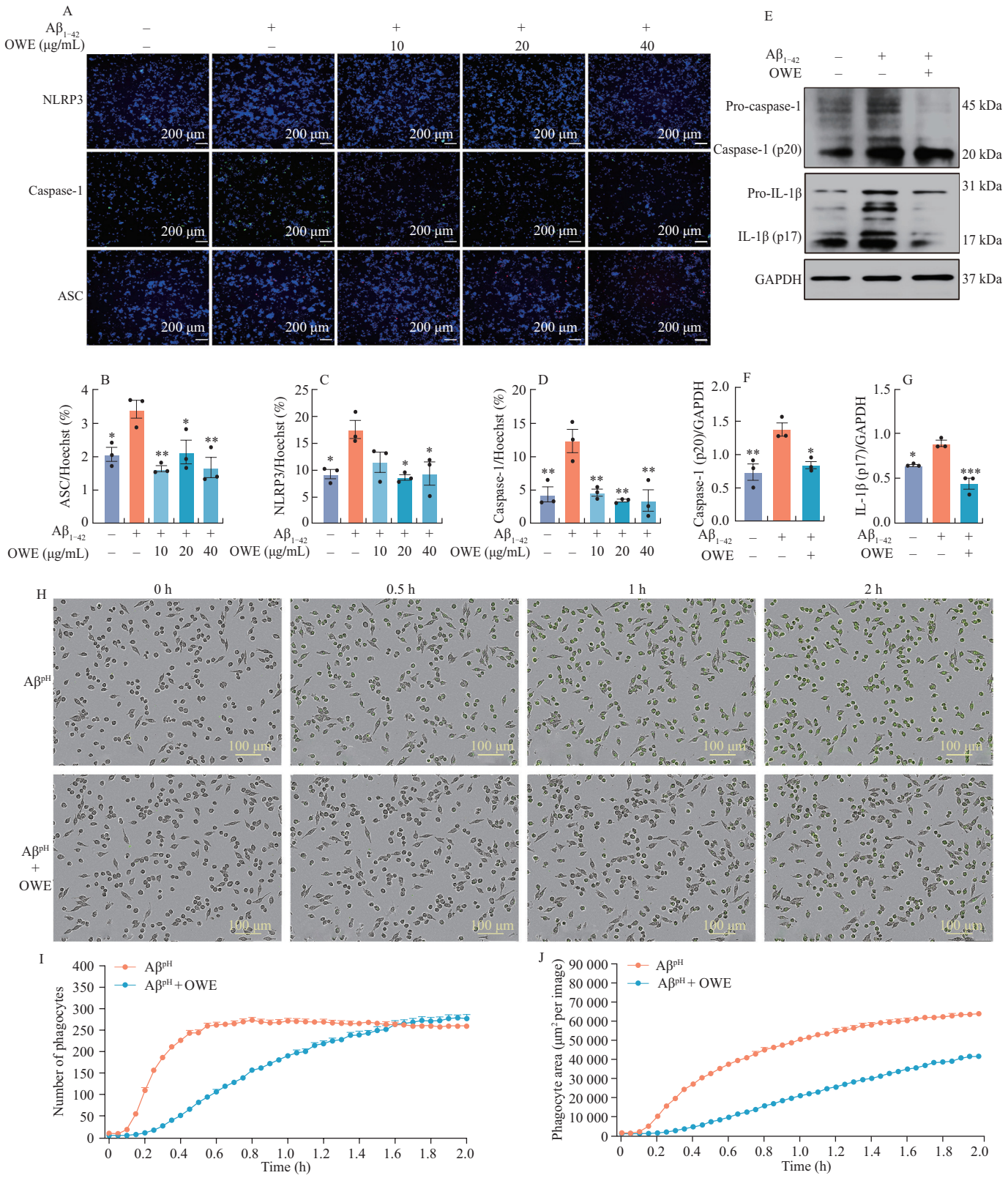


Fig. 3 OWE inhibits the activation of NLRP3 inflammasome and cell phagocytosis in $A\beta_{1-42}$-stimulated BV-2 cells. (A) Representative images of BV-2 cells transiently transfected with pEGFP-N1-NLRP3, pEGFP-N1-caspase-1, or pmCherry-C1-ASC and Hoechst-stained, stimulated with $A\beta_{1-42}$ in the presence or absence of OWE at specified concentrations. Magnification 10×, scale bar 200 μm. (B–D) Relative percentage of ASC, NLRP3, and caspase-1 to Hoechst staining. (E) Representative Western blot images of caspase-1, IL-1β, and GAPDH, with original and non-processed Western blot images available in Fig. S2. (F, G) Relative protein expressions of caspase-1 (p20) and cleaved-IL-1β to GAPDH, respectively. (H) White light and fluorescence images of $A\beta^{pH}$-stimulated BV-2 cells treated with or without OWE (40 μg/mL) over times of 0, 0.5, 1, and 2 h. Magnification 20×, scale bar 100 μm. (I, J) Number of phagocytes in $A\beta^{pH}$-stimulated BV-2 cells treated with or without OWE within 2 h. Data are expressed as mean ± SD. $^*P < 0.05$, $^{**}P < 0.01$, $^{***}P < 0.001$ *vs*. $A\beta_{1-42}$ postitive control group.

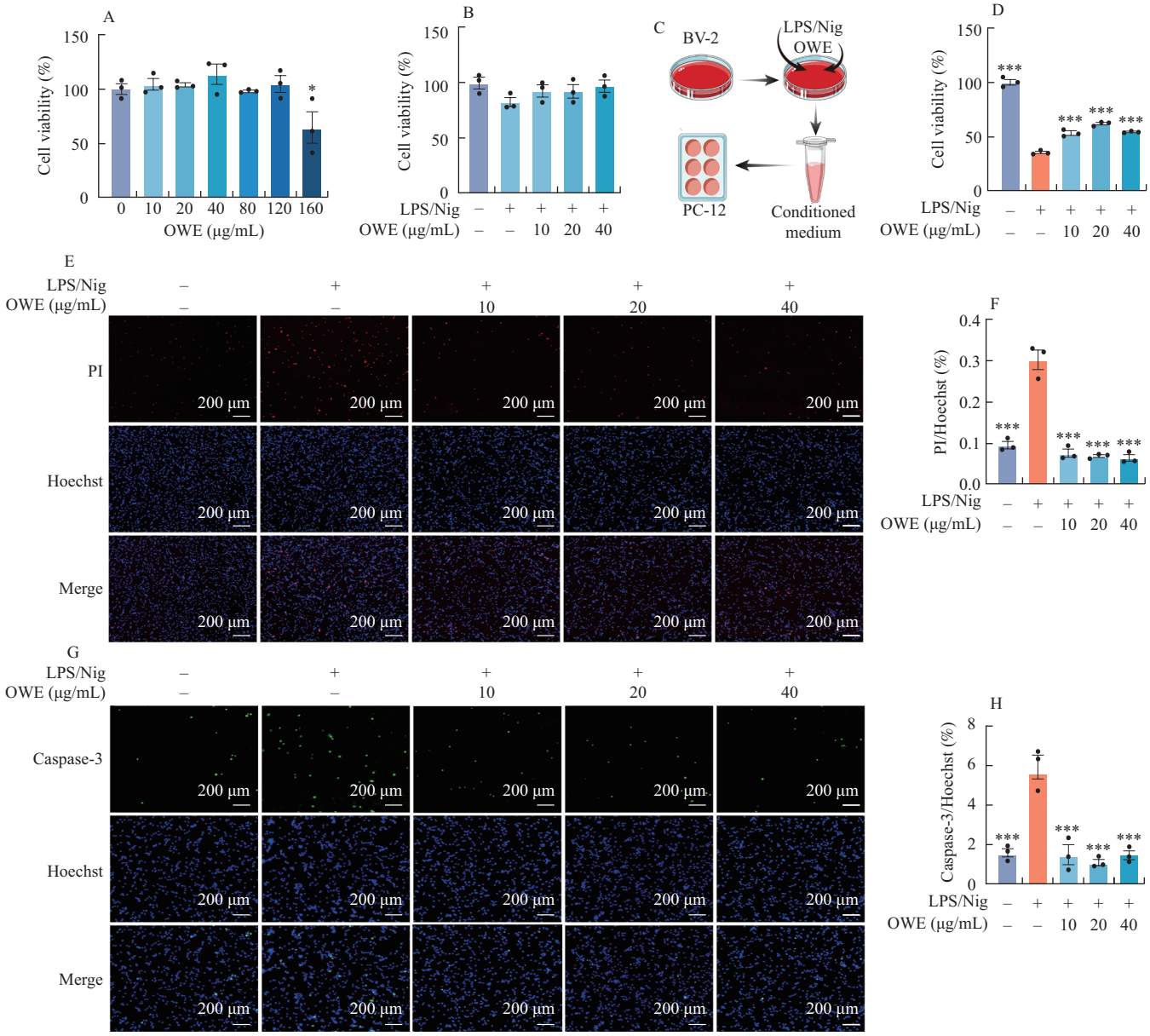


Fig. 4 OWE ameliorates the cytokines-containing conditioned medium-induced death in PC12 cells. (A, B) Cell viability of PC12 cells treated with OWE or with LPS/Nig in the presence or absence of OWE at indicated concentrations. *$P < 0.05$ *vs*. control group. (C) Schematic diagram of the treatment of PC12 cells with conditioned medium from BV-2 cells stimulated with LPS/Nig in the presence or absence of OWE. (D) Cell viability of PC12 cells treated with the conditioned medium. (E) Representative images of Hoechst/PI-stained PC12 cells treated with conditioned medium. Magnification 10×, scale bar 200 μm. (F) Relative ratio of PI to Hoechst, measuring cell death. (G) Representative images showing caspase-3 expression in PC12 cells treated with conditioned medium. Magnification 10×, scale bar 200 μm. (H) Relative ratio of caspase-3 to Hoechst, highlighting apoptotic activity. The data are expressed as mean ± SD. *$P < 0.05$, **$P < 0.01$, ***$P < 0.001$ *vs*. LPS/Nig positive control group.

in autophagosome-lysosome fusion. Following the administration of Baf, the GFP/RFP ratio in cells treated with OWE showed partial restoration, further confirming the role of OWE in enhancing autophagic flux. Additionally, TEM provided morphological evidence of autophagic activation, revealing an increased number of autophagic vacuoles (autophagosomes and autolysosomes) in OWE-treated U87 cells compared to control cells (Fig. 5I). Together, these findings demonstrate that OWE activates autophagy *in vitro*. We further explored the molecular mechanisms underlying the autophagy activation in BV-2 cells, focusing on the AMPK-PI3K/AKT/mTOR signaling pathway. Western blot analysis assessed the expression levels of key proteins within this pathway. Our results showed that OWE significantly increased the phosphorylation of AMPK (p-AMPK) while concurrently decreasing the phosphorylation levels of PI3K (p-PI3K), AKT (p-AKT), and mTOR (p-mTOR) (Figs. 5J–N). These findings indicate that OWE can modulate the AMPK-PI3K/AKT/mTOR signaling pathway. To further validate whether OWE induces autophagy through AMPK activation, we employed the specific AMPK inhibitor CC. Treatment with CC significantly inhibited the increase in GFP-LC3 puncta in stable GFP-RFP-LC3 U87 cells induced by OWE (Figs. 5O and P). Additionally, the increased LC3-II/LC3-I ratio in BV-2 cells facilitated by OWE was also notably suppressed by CC treatment (Figs. 5Q and R). Collectively, these findings provide substantial evidence that OWE activates autophagy in BV-2 cells by regulating the AMPK-PI3K/AKT/mTOR signaling pathway.

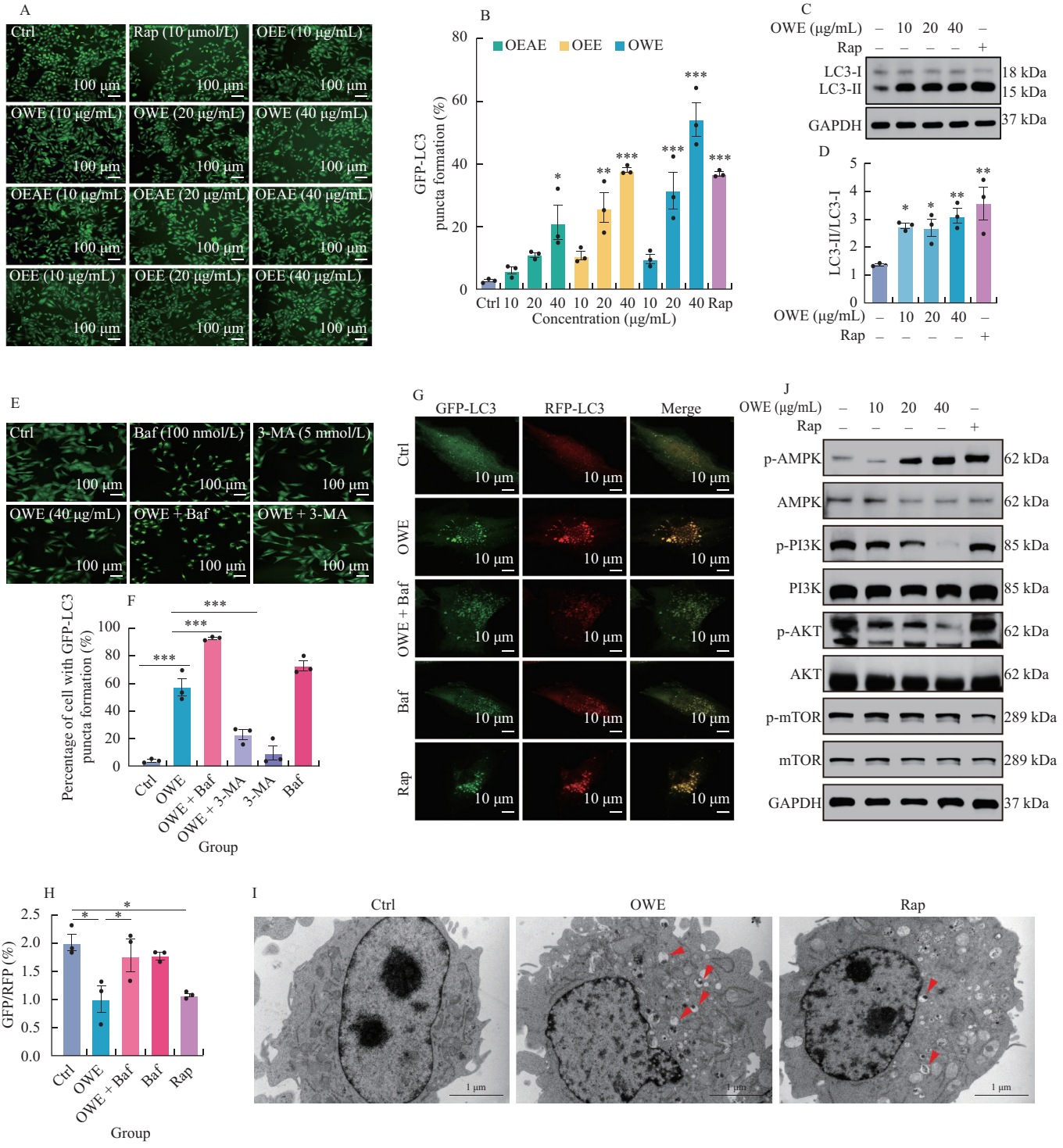


Fig. 5 OWE activates autophagy via regulating the AMPK-PI3K/AKT/mTOR signaling pathway. (A) Representative images of stable GFP-RFP-LC3 U87 cells showing GFP-LC3 puncta formation after treatment with OWE, OEAE, OEE, and Rap at indicated concentrations. Magnification 20×, scale bar 100 μm. (B) Percentage of cells with GFP-LC3 puncta. (C) Representative Western blot images of LC3 and GAPDH in BV-2 cells treated with OWE and Rap at specified concentrations. Original and non-processed Western blot images are available in Fig. S3. (D) Ratio of LC3-II to LC3-I. *$P < 0.05$, **$P < 0.01$, ***$P < 0.001$ *vs*. control group. (E) Representative images of stable GFP-RFP-LC3 U87 cells depicting GFP-LC3 puncta formation when treated with OWE in the presence or absence of Baf and 3-MA at indicated concentrations. Magnification 20×, scale bar 100 μm. (F) Percentage of cells with GFP-LC3 puncta under these conditions. (G) Representative images displaying GFP-LC3 and RFP-LC3 puncta formation in stable GFP-RFP-LC3 U87 cells treated with Rap and OWE in the presence or absence of Baf at specified concentrations. Magnification 63×, scale bar 10 μm. (H) Ratio of GFP to RFP. (I) Representative TEM images showing autophagic vacuoles (indicated by red arrows) in BV-2 cells treated with OWE and Rap compared to control cells. Magnification 10 000×, scale bar 1 μm. (J) Representative Western blot images showing p-AMPK, AMPK, p-PI3K, PI3K, p-AKT, AKT, p-mTOR, mTOR, and GAPDH in BV-2 cells treated with OWE and Rap at specified concentrations. Original and non-processed Western blot images are available in Fig. S4. (K–N) Ratios of p-AMPK/AMPK, p-PI3K/PI3K, p-AKT/AKT, and p-mTOR/mTOR. (O) Representative images of stable GFP-RFP-LC3 U87 cells showing GFP-LC3 puncta formation after treatment with OWE in the presence or absence of CC at indicated concentrations. Magnification 20×, scale bar 100 μm. (P) Percentage of cells with GFP-LC3 puncta. (Q) Representative Western blot images of LC3 and GAPDH in BV-2 cells treated with OWE in the presence or absence of CC. Original and non-processed Western blot images are available in Fig. S5. (R) Ratio of LC3-II to LC3-I. The data are expressed as mean ± SD. *$P < 0.05$, **$P < 0.01$, ***$P < 0.001$.

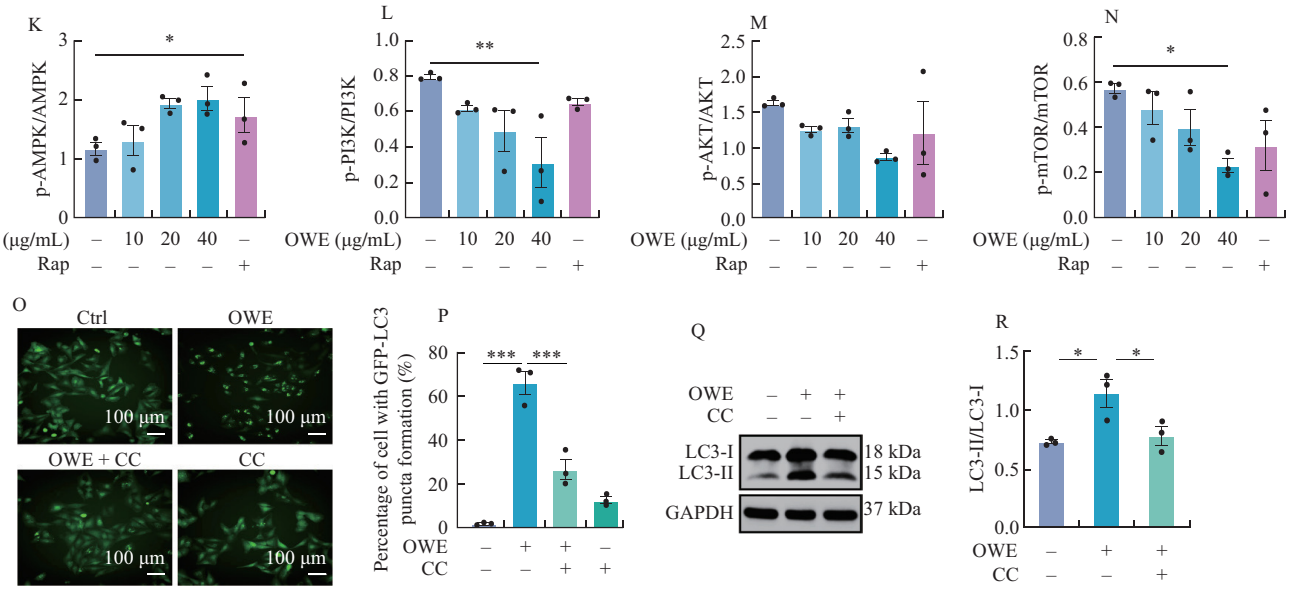


Fig. 5 (*Continued*)

3.6 OWE inhibits the NLRP3 inflammasome and pyroptosis via autophagy induction

To validate whether OWE suppresses NLRP3 inflammasome activation through the induction of autophagy, we utilized the autophagy inhibitor Baf and the AMPK inhibitor CC. Western blot analysis was employed to measure the expression levels of inflammasome-related proteins. Our results revealed that OWE significantly reduced the expression of NLRP3 and ASC, as well as cleaved caspase-1, N-GSDMD, and mature IL-1β (Figs. 6A–F). However, the inhibition of these protein expressions was reversed upon the application of Baf and CC. Additionally, transient transfection of BV-2 cells with pEGFP-N1-NLRP3, pEGFP-N1-caspase-1, or pmCherry-C1-ASC followed by fluorescence microscopy showed that both Baf and CC could reverse the inhibitory effects of OWE on the fluorescence intensity of GFP and mCherry (Figs. 6G–J). We also used YO-PRO-1/Eth-D2 staining to examine the formation of GSDMD pores on the BV-2 cell membrane. The results indicated that the inhibition of GSDMD pore formation by OWE was weakened by the application of Baf (Figs. 6K and L). Concurrently, OWE significantly increased GFP-LC3 puncta formation and its colocalization with NLRP3 protein (Fig. 6M), suggesting that OWE inhibits the NLRP3 inflammasome via autophagy induction. Therefore, these findings underscore that OWE inhibits NLRP3 inflammasome activation and subsequent pyroptosis in LPS/Nig-stimulated BV-2 cells primarily through the induction of autophagy.

3.7 OWE ameliorates Aβ-induced paralysis and cell death in C. elegans via autophagy induction

Our investigation into the therapeutic potential of OWE for mitigating Aβ-induced effects utilized the model organism *C. elegans* to demonstrate its efficacy in enhancing autophagy and reducing Aβ toxicity. Evidence of autophagy induction was observed through the increased formation of GFP::LGG-1 puncta in DA2123 worms treated with OWE and Rap (Figs. 7A and B). Concurrently, reduced p62 accumulation in BC12921 worms indicated enhanced autophagic flux (Figs. 7C and D). In CL4176 worms, which express human Aβ and are predisposed to paralysis, OWE treatment markedly decreased the incidence of paralysis (Figs. 7E and F). This protective effect was attenuated when autophagy was inhibited by feeding the worms *lgg-1* RNAi bacteria, underscoring the critical role of autophagy (Figs. 7G and H). Additionally, fluorescence staining of worm intestines with uranine and acridine orange revealed improved cellular integrity in OWE-treated groups, suggesting a reduction in cell death (Fig. 7I). Furthermore, survival curve analysis (Fig. S7) and DAPI staining (Fig. S8) showed that OWE significantly increased the survival rate and cell viability of PA14-treated N2 worms, while the beneficial effects of OWE were counteracted by *lgg-1* RNAi bacteria. These findings collectively highlight OWE's potential as a therapeutic agent for AD, leveraging its ability to activate autophagy and mitigate paralysis and cell death induced by Aβ.

3.8 OWE inhibits the activation of NLRP3 inflammasome via autophagy induction in 3xTg-AD mice

Our investigation into the neuroprotective effects of OWE in a 3xTg-AD mouse model of AD revealed novel insights into its mechanism of action, specifically through the modulation of the NLRP3 inflammasome pathway via the induction of autophagy. Behavioral analysis using the MWM test demonstrated significant cognitive improvements in OWE-treated mice, with representative swimming trajectory images (Fig. 8A), quantified swimming lengths (Fig. 8B), escape latencies (Fig. 8C), and average swimming speeds (Fig. S9) indicating enhanced memory and learning compared to untreated 3xTg-AD mice. At the molecular level, immunofluorescence staining showed reduced glial activation and maintained neuronal integrity in OWE-treated groups, as evidenced by the quantification of $GFAP^+$, $Iba\text{-}1^+$, and $NeuN^+$ cells (Figs. 8D–G). Furthermore, the colocalization of LC3 and NLRP3 suggested a direct interaction between autophagy and NLRP3 inflammasome activation pathways (Figs. 8H and I). Western blot analysis provided additional

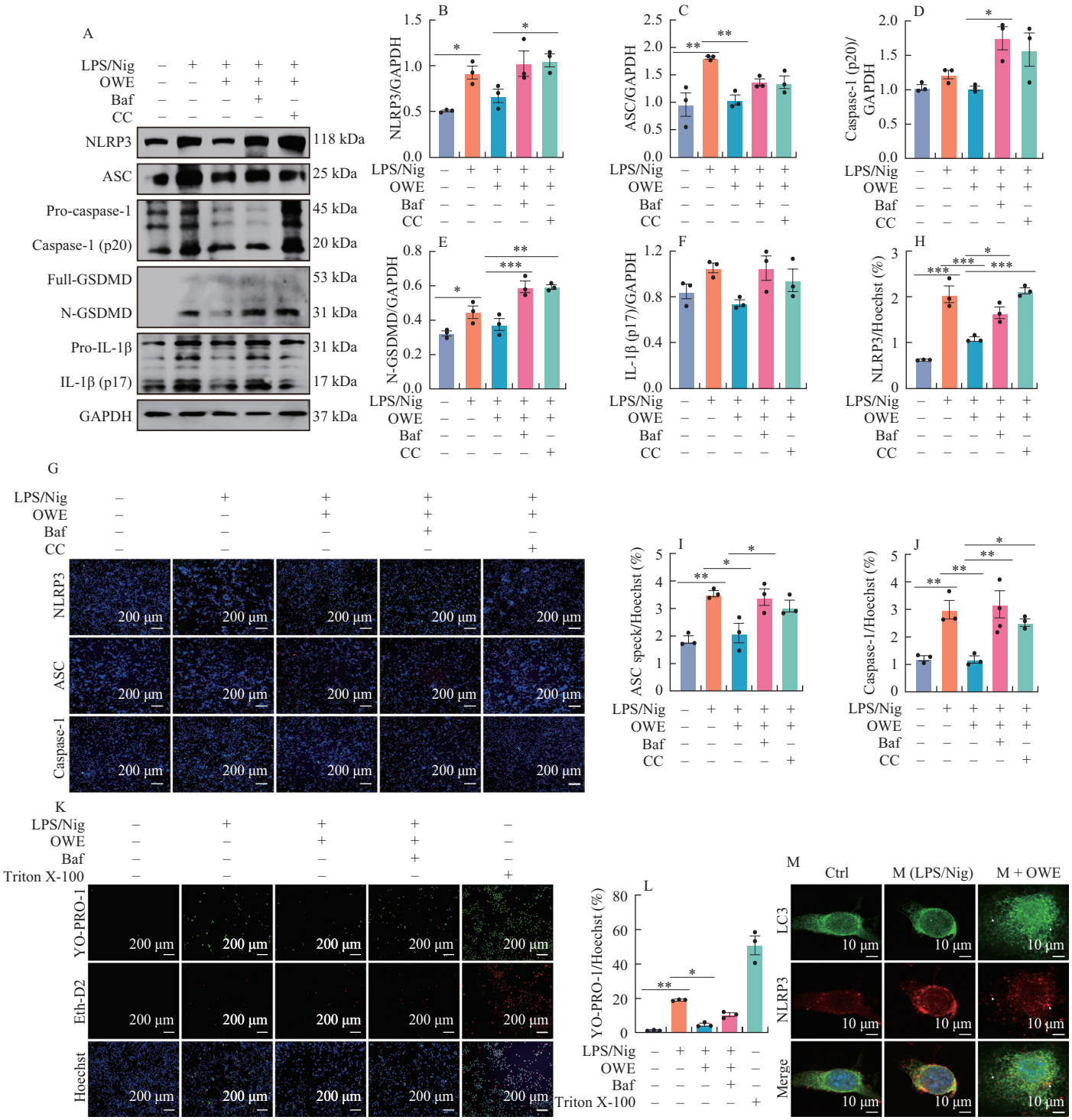


Fig. 6 OWE inhibits the NLRP3 inflammasome and pyroptosis via autophagy induction. (A) Representative Western blot images showing levels of NLRP3, ASC, caspase-1, GSDMD, IL-1β, and GAPDH in LPS/Nig-stimulated BV-2 cells treated with OWE in the presence or absence of Baf and CC at indicated concentrations. Original and non-processed Western blot images are available in Fig. S6. (B–F) Bar charts display the relative protein expressions of NLRP3, ASC, caspase-1 (p20), N-GSDMD, and cleaved-IL-1β to GAPDH, respectively. (G) Representative images of BV-2 cells transiently transfected with pEGFP-N1-NLRP3, pEGFP-N1-caspase-1, or pmCherry-C1-ASC and Hoechst-stained, stimulated with LPS/Nig in the presence or absence of OWE, with or without Baf and CC at specified concentrations. Magnification 10×, scale bar 200 μm. (H–J) Relative percentage of NLRP3, ASC, and caspase-1 to Hoechst. (K) Representative images of YO-PRO-1/EthD-2-stained BV-2 cells following LPS/Nig stimulation and OWE treatment in the presence or absence of Baf. Triton X-100-treated cells, without LPS/Nig stimulation, were used as the positive control. Magnification 10×, scale bar 200 μm. (L) Ratio of YO-PRO-1 to Hoechst in BV-2 cells. (M) Representative confocal images demonstrating the colocalization of LC3 with NLRP3 in LPS/Nig-stimulated BV-2 cells treated with or without 40 μg/mL OWE. Magnification 63×, scale bar 10 μm. The data are expressed as mean ± SD. $^{*}P < 0.05$, $^{**}P < 0.01$, $^{***}P < 0.001$.

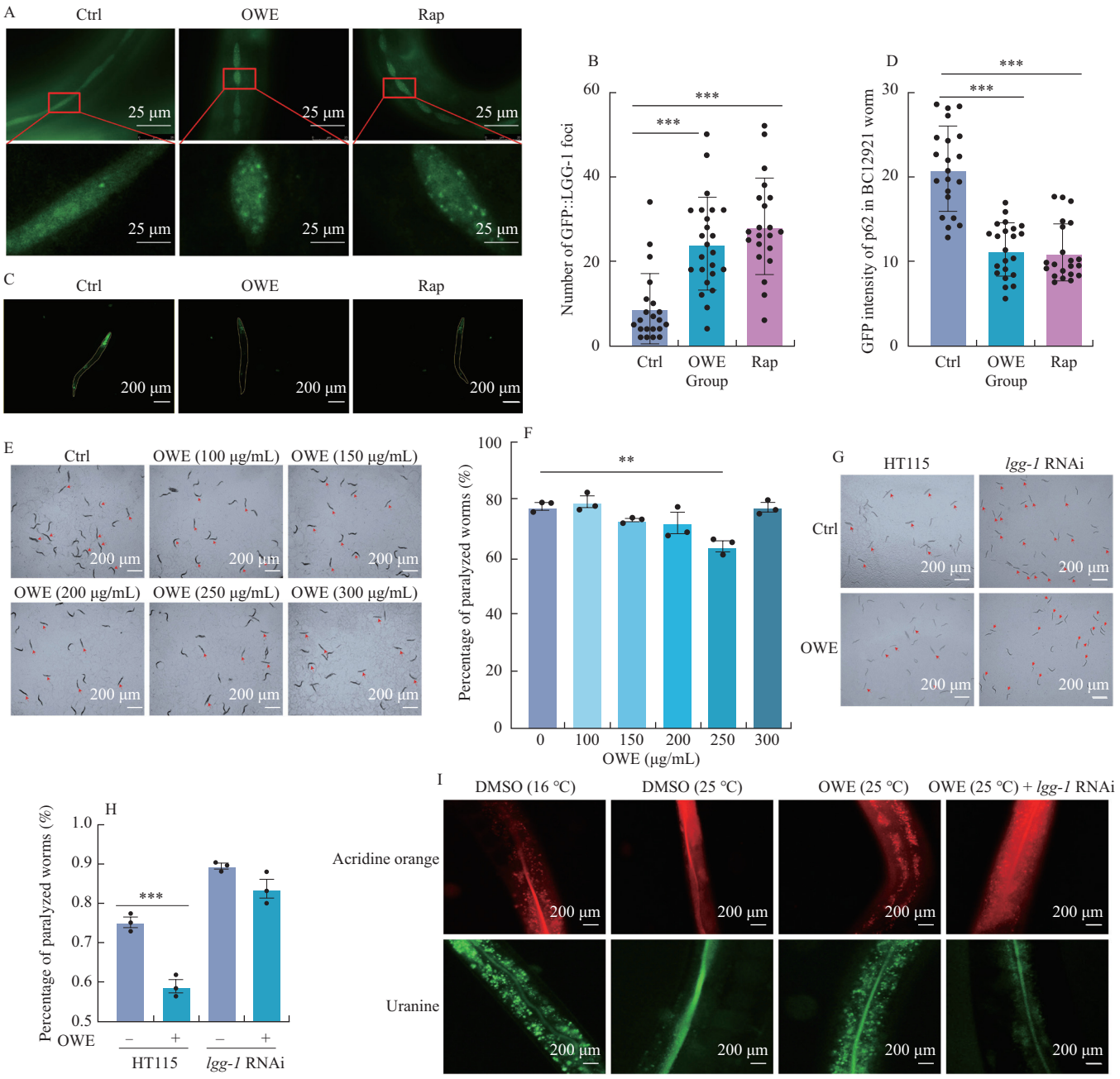


Fig. 7 OWE ameliorates Aβ-induced paralysis and pyroptosis in *C. elegans* via autophagy induction. (A) Representative images showing GPF::LGG-1 puncta formation in DA2123 worms treated with OWE and Rap at specified concentrations. Magnification 20×, scale bar 100 μm. (B) The bar chart indicates the number of GFP::LGG-1 foci in DA2123 worms. (C) Representative images displaying the expression of p62 in BC12921 worms. Magnification 10×, scale bar 200 μm. (D) GFP intensity of p62 in BC12921 worms. (E) Representative images depicting the paralysis of CL4176 worms treated with OWE at indicated concentrations. Magnification 10×, scale bar 200 μm. (F) Percentage of paralyzed worms. (G) Representative images showing the paralysis of OWE-treated CL4176 worms feeding with HT115 and *lgg-1* RNAi bacteria. Magnification 10×, scale bar 200 μm. (H) Percentage of paralyzed worms in the treated groups. (I) Representative fluorescence images showing uranine- and acridine orange-labeled intestines in CL4176 worms. Magnification 20×, scale bar 100 μm. The data are expressed as mean ± SD. *$P < 0.05$, **$P < 0.01$, ***$P < 0.001$.

molecular insights, revealing significantly reduced expression levels of NLRP3, ASC, cleaved caspase-1, N-GSDMD, and cleaved IL-1β, along with decreased phosphorylation of key autophagy-related signaling proteins, including mTOR, and enhanced activation of AMPK (Figs. 8J–Q). The elevated ratios of LC3-II to LC3-I in OWE-treated mice confirmed enhanced autophagic flux (Fig. 8R). These findings demonstrate that OWE effectively inhibits NLRP3 inflammasome activation in 3xTg-AD mice through autophagy induction, underscoring its potential as a novel therapeutic strategy for AD.

4. Discussion

The pathogenesis of AD is intricately linked with chronic neuroinflammation and neuronal death, processes in which the NLRP3 inflammasome and pyroptosis play critical roles[16,26-42]. Targeting these pathways holds promise for developing novel therapeutic interventions. Natural products have long been valued for their therapeutic potential, offering a vast reservoir of bioactive compounds with unique structural diversity and biological activities[45-46]. These

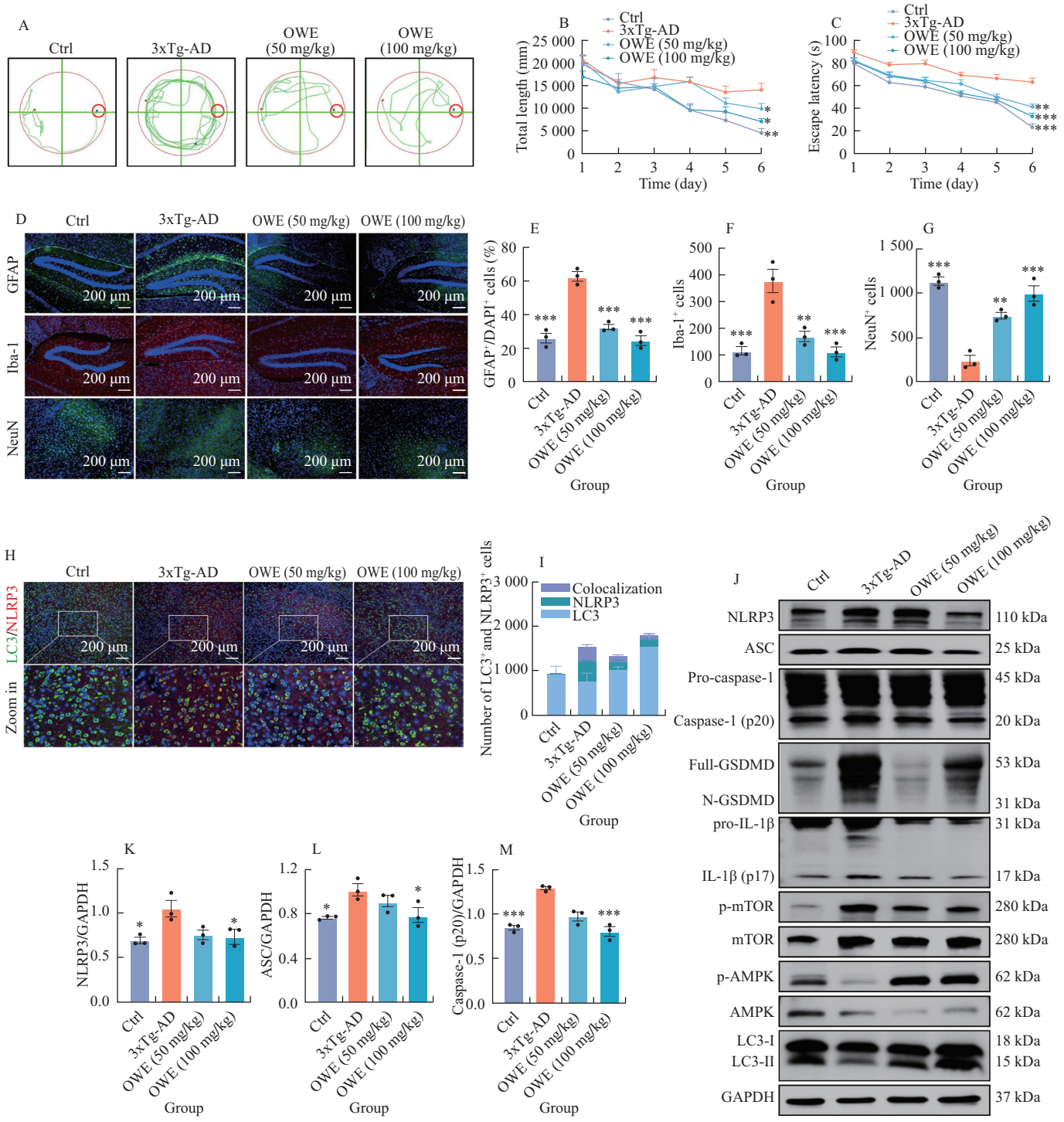


Fig. 8 OWE inhibits the activation of NLRP3 inflammasome via autophagy induction in 3xTg-AD mice. (A) Representative swimming trajectory images of mice during the MWM test. (B) Total length of swimming and (C) escape latencies of mice. (D) Representative immunofluorescence images displaying GFAP, Iba-1, and NeuN in the brain tissue of mice treated with or without OWE at indicated concentrations. Magnification 10×, scale bar 200 μm. (E–G) Number of GFAP$^+$, Iba-1$^+$, and NeuN$^+$ cells in the brain tissue. (H) Representative immunofluorescence images showing the colocalization of LC3 and NLRP3 in the brain tissue, suggesting interactions between autophagy and NLRP3 inflammasome. The area in the white frame is magnified below. Magnification 10×, scale bar 200 μm. (I) Number of LC3$^+$ and NLRP3$^+$ cells, and their colocalization in the brain tissue. (J) Representative Western blot images of NLRP3, ASC, caspase-1, GSDMD, IL-1β, p-mTOR, mTOR, p-AMPK, AMPK, LC3, and GAPDH in the brain tissue of mice. Original and non-processed Western blot images are available in Fig. S10. (K–R) Relative protein expressions of NLRP3, ASC, caspase-1 (p20), N-GSDMD, IL-1β (p17), p-mTOR/mTOR, p-AMPK/AMPK and LC3-II/LC3-I. The data are expressed as mean ± SD. *P < 0.05, **P < 0.01, ***P < 0.001 *vs*. 3xTg-AD group.

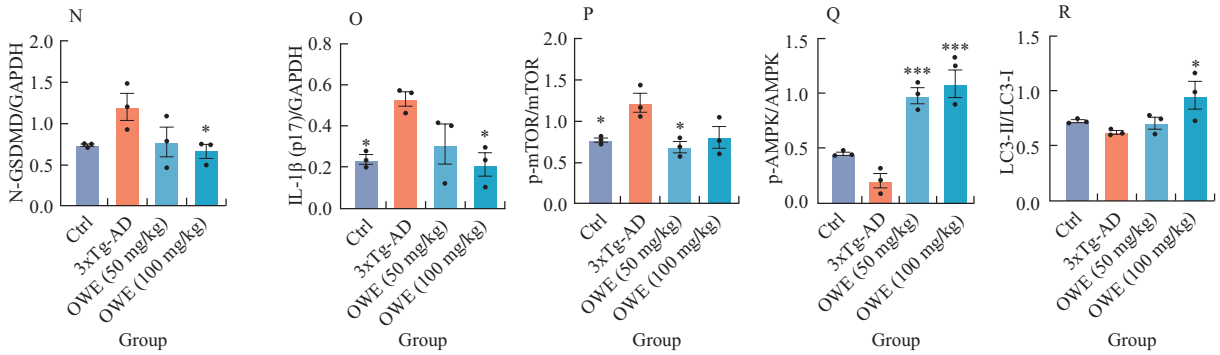


Fig. 8 (*Continued*)

natural compounds often exhibit multi-targeted effects, making them advantageous for treating complex diseases like AD[47]. In this study, we screened a library of herbal extracts to identify potential inhibitors of NLRP3 inflammasome activation and discovered that OWE is a modulator of neuroinflammation and autophagy, offering a new perspective on AD treatment.

Our study provides significant insights into the therapeutic potential of OWE in modulating neuroinflammation and pyroptosis via inhibition of the NLRP3 inflammasome. These results contribute to the growing body of evidence supporting the role of natural compounds in regulating inflammatory pathways, particularly through the induction of autophagy (Fig. 9)[48]. Specifically, our findings align with the established understanding that autophagy plays a crucial role in mitigating inflammatory responses and cellular stress by degrading and recycling damaged cellular components. Furthermore, the study underscores the importance of the AMPK-PI3K/AKT/mTOR signaling pathway in autophagy regulation and its downstream effects on inflammasome activity. Consistent with prior research, our results affirm that the NLRP3 inflammasome is a critical mediator of neuroinflammation and pyroptosis in microglial cells. Previous studies have demonstrated the involvement of NLRP3 in various neurodegenerative diseases, including AD[17]. However, our study diverges by focusing specifically on the efficacy of OWE, which has not been extensively explored in this context. The identification of bioactive constituents such as ellagic acid, gallic acid, quercetin, and oenothein B in OWE highlights a unique combination of compounds that collectively contribute to its potent anti-inflammatory and autophagy-inducing effects. This combination has not been previously reported, adding novel insights to the field of natural product pharmacology.

Using an *in vitro* model of BV-2 microglial cells activated by LPS/Nig, a library of 288 herbal extracts and compounds were screened. Pyroptosis-specific markers—cleaved caspase-1 and N-GSDMD—were quantified by Western blotting, and cell death was assessed using Hoechst/PI and YO-PRO-1/Eth-D2 staining instead of TUNEL staining. We found that OWE treatment significantly inhibits pyroptosis in LPS/Nig-treated BV-2 cells. This aligns with existing research indicating that targeting the NLRP3 inflammasome can reduce neuroinflammation and neuronal damage in AD. The low cytotoxicity and high efficacy of OWE make it a promising candidate for further development. Additionally, the preliminary chemical profiling of OWE identified several bioactive compounds, including ellagic acid, gallic acid, quercetin, and oenothein B[33]. These components likely contribute to the observed protective effects of OWE[34]. Future studies should focus on isolating and characterizing these specific active constituents to further understand their roles in inhibiting pyroptosis in microglial cells. Furthermore, to ensure reproducibility, we employed consistent experimental conditions, including standardized drug concentrations, treatment durations, and uniform imaging and quantification settings. The reliability of our results was further supported by replicating experiments in independent biological replicates, reducing potential variability.

The clinical implications of our findings are profound. By demonstrating that OWE can inhibit NLRP3 inflammasome activation and pyroptosis, our study suggests that OWE could be developed as a therapeutic agent for neuroinflammatory conditions, including AD. The ability of OWE to enhance cell viability, reduce inflammatory cytokine production, and modulate microglial phagocytic activity indicates its potential to mitigate neuroinflammation and protect neuronal integrity. This could translate into improved clinical outcomes for patients with neurodegenerative diseases. Additionally, the inhibition of conditioned medium-induced neuronal death in PC12 cells suggests that OWE could protect against secondary neuronal damage caused by microglial activation, further highlighting its therapeutic promise.

Autophagy, a cellular process critical for removing damaged organelles and proteins, has been shown to inhibit the activity of the NLRP3 inflammasome[26,44-51]. To investigate the potential of OWE to induce autophagy, we conducted a series of experiments focusing on its effects in BV-2 microglial cells and stable GFP-RFP-LC3 U87 cells. The enhancement of autophagic flux, as evidenced by increased LC3-II/LC3-I ratios and autophagosome formation, underscores the role of OWE in promoting cellular homeostasis. This is particularly relevant in AD, where impaired autophagy is a well-documented issue[52]. AMPK activation and concurrent inhibition of PI3K, AKT, and mTOR phosphorylation indicate a shift towards a cellular state favoring autophagy. Given the critical role of mTOR in regulating autophagy, its inhibition by OWE suggests a robust mechanism for enhancing autophagic activity. Collectively, these findings provide substantial evidence that OWE activates autophagy in BV-2 cells via modulation of the AMPK-PI3K/AKT/mTOR signaling pathway. To validate whether OWE suppresses NLRP3 inflammasome activation through the induction of autophagy, we utilized the autophagy inhibitor Baf and the AMPK inhibitor CC. Western blot analysis and fluorescence microscopy observation showed that both Baf and CC could reverse the inhibitory effects of OWE on the expression of NLRP3 and ASC, as well as cleaved caspase-1, N-GSDMD,

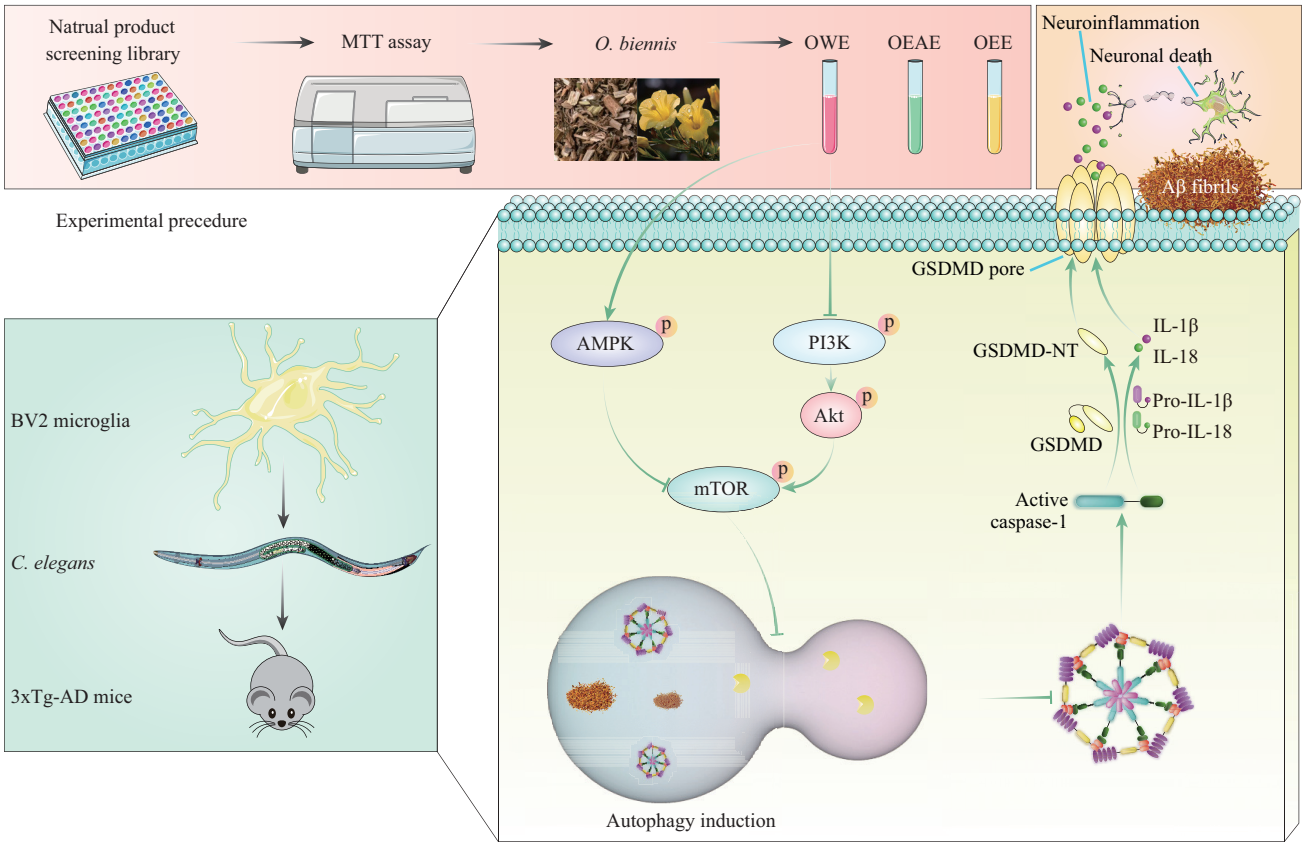


Fig. 9 Schematic diagram of the study. This diagram illustrates the comprehensive pathway through which OWE exerts its therapeutic effects in AD. Initial screening from a natural product library revealed OWE's ability to significantly enhance cell viability in LPS/Nig-stimulated BV-2 cells. Subsequent research in BV-2 cells, *C. elegans*, and 3xTg-AD mice models showed that OWE effectively inhibits Aβ-induced NLRP3 inflammasome activation. This inhibition is mediated by autophagy through the AMPK-PI3K/Akt/mTOR signaling pathway, underscoring OWE's potential to reduce neuroinflammation and prevent neuronal death.

and mature IL-1β. Moreover, immunofluorescence assays revealed significant increases in GFP-LC3 puncta formation and its colocalization with NLRP3 protein. Therefore, autophagy induction directly contributes to the inhibition of the NLRP3 inflammasome in BV-2 cells, providing a dual mechanism of action for OWE in combating neuroinflammation and proteinopathy in AD. To ensure the reproducibility of this mechanism, all experimental conditions for detecting autophagy, including autophagic flux assays and inhibitor validation, were conducted with standardized imaging settings and automated fluorescence quantification, reducing observer bias. The consistency of autophagic induction was further validated across different cell lines and *in vivo* models, reinforcing the robustness of our findings.

To further explore the therapeutic potential of OWE in activating autophagy and mitigating Aβ-induced pathology and the activation of NLRP3 inflammasome, we utilized *C. elegans* to demonstrate its efficacy in enhancing autophagy and reducing Aβ toxicity. Autophagy induction was evidenced by increased formation of GFP::LGG-1 puncta in DA2123 worms and reduced p62 accumulation in BC12921 worms. In CL4176 worms, OWE treatment markedly decreased the incidence of paralysis. This protective effect was attenuated when autophagy was inhibited by feeding the worms with *lgg-1* RNAi bacteria, underscoring autophagy's critical role. Additionally, fluorescence staining of worm intestines with uranine and acridine orange revealed improved cellular integrity in OWE-treated groups, suggesting a reduction in cell death. These findings collectively highlight OWE's potential as a therapeutic agent for AD and related conditions, leveraging its ability to activate autophagy and mitigate paralysis and cell death induced by Aβ. To further ensure the reproducibility of our findings in *C. elegans*, imaging conditions, fluorescence quantification parameters, and RNAi treatment protocols were standardized across all experiments. The results were independently validated by blinded observers, minimizing potential bias in data interpretation.

In our investigation into the neuroprotective effects of OWE in a 3xTg-AD mouse model of AD, we focused on the modulation of the NLRP3 inflammasome pathway through the induction of autophagy. The MWM test revealed improvements in cognitive function in OWE-treated mice compared to untreated 3xTg-AD mice. At the molecular level, immunofluorescence staining showed that OWE could reduce glial activation and maintain neuronal integrity in 3xTg-AD mice. The colocalization of LC3 and NLRP3 was assessed, the results indicated that OWE inhibits the activation of NLRP3 inflammasome via autophagy induction. Furthermore, Western blot analysis provided additional insights into the molecular mechanisms that OWE enhanced autophagic flux and inhibited the activation of NLRP3 inflammasome. Therefore, these findings demonstrate that OWE effectively inhibits the activation of the NLRP3 inflammasome in 3xTg-AD mice, primarily through the induction of autophagy. This comprehensive evidence underscores OWE's therapeutic potential

in alleviating cognitive deficits and neuropathological features of AD by modulating autophagy and inflammasome pathways. To ensure the reproducibility of *in vivo* findings, we employed rigorous experimental controls, including age- and sex-matched mice, consistent housing conditions, and standardized drug administration protocols. Behavioral assessments were conducted by experimenters blinded to the treatment groups to reduce potential bias.

Despite these promising findings, several limitations must be addressed in future studies. First, while our study demonstrates the efficacy of OWE *in vitro* and animal models, clinical trials are necessary to confirm its safety and effectiveness in humans. Second, the exact bioactive components responsible for the observed effects need to be isolated and characterized to understand their specific mechanisms of action. Third, long-term studies are required to evaluate the potential side effects and optimal dosage of OWE. Future research should also explore the combinatory effects of OWE with other therapeutic agents to enhance its efficacy and broaden its application in AD treatment. Additionally, investigating the role of OWE in other neuroinflammatory conditions could provide further insights into its therapeutic potential.

5. Conclusion

In conclusion, this study provides compelling evidence that OWE exhibits significant neuroprotective effects in AD. By inhibiting the NLRP3 inflammasome through the induction of autophagy, mediated via the AMPK-PI3K/AKT/mTOR pathway, OWE effectively mitigates neuroinflammation and neuronal damage. These findings make a notable contribution to the current understanding of AD pathology, highlighting the critical role of autophagy in regulating neuroinflammatory responses. Furthermore, the identification of OWE as a multi-targeted therapeutic agent offers a promising new approach for the treatment of AD. This research not only advances theoretical knowledge but also paves the way for practical applications in developing novel therapeutic strategies for neurodegenerative diseases. The demonstrated efficacy of OWE underscores its potential to significantly impact the future of AD treatment, emphasizing the need for further clinical investigation.

Declaration of competing interest

The authors declare that they have no known competing financial interests or personal relationships that could have appeared to influence the work reported in this paper.

Acknowledgment

We would like to thank AJE (www.aje.cn) for English language editing. This work was supported by the National Natural Science Foundation of China (81903829), the Open Project from the State Key Laboratory of Traditional Chinese Medicine Syndrome (SKLKY2024B0006), the Foundation of Institute of Traditional Chinese Medicine Health Industry, China Academy of Chinese Medical Sciences (ZYTS-2025011), Ziyang Central Hospital-Southwest Medical University Science and Technology Strategic Cooperation (2025ZYXNYD13), the Open Fund of Innovation Center for Basic Research on Metabolic Cardiovascular Diseases, Southwest Medical University (xnykdxcxzx-2025-10), and the Joint Project of Luzhou Municipal People's Government and Southwest Medical University (2024LZXNYDJ026).

Appendix A. Supplementary data

Supplementary data associated with this article can be found, in the online version, at http://doi.org/10.26599/FSHW.2025.9250595.

References

[1] R. Fecker, V. Buda, E. Alexa, et al., Phytochemical and biological screening of *Oenothera biennis* L. hydroalcoholic extract, Biomolecules 10 (2020) 818. https://doi.org/10.3390/biom10060818.

[2] S. Granica, M.E. Czerwińska, J.P. Piwowarski, et al., Chemical composition, antioxidative and anti-inflammatory activity of extracts prepared from aerial parts of *Oenothera biennis* L. and *Oenothera paradoxa* Hudziok obtained after seeds cultivation, J. Agric. Food Chem. 61 (2013) 801-810. https://doi.org/10.1021/jf304002h.

[3] J. Zaugg, O. Potterat, A. Plescher, et al., Quantitative analysis of anti-inflammatory and radical scavenging triterpenoid esters in evening primrose seeds, J. Agric. Food Chem. 54 (2006) 6623-6628. https://doi.org/10.1021/jf0611466.

[4] M.A. Farag, A. Reda, M. Nabil, et al., Evening primrose oil: a comprehensive review of its bioactives, extraction, analysis, oil quality, therapeutic merits, and safety, Food Funct. 14 (2023) 8049-8070. https://doi.org/10.1039/d3fo01949g.

[5] M. Sharifi, N. Nourani, S. Sanaie, et al., The effect of *Oenothera biennis* (Evening primrose) oil on inflammatory diseases: a systematic review of clinical trials, BMC Complement. Med. Ther. 24 (2024) 89. https://doi.org/10.1186/s12906-024-04378-5.

[6] S. Selek, M. Esrefoglu, I. Meral, et al., Effects of *Oenothera biennis* L. and *Hypericum perforatum* L. extracts on some central nervous system myelin proteins, brain histopathology and oxidative stress in mice with experimental autoimmune encephalomyelitis, Biotech. Histochem. 94 (2019) 75-83. https://doi.org/10.1080/10520295.2018.1482001.

[7] M. Guo, F. Zhu, W. Qiu, et al., High-throughput screening for amyloid-β binding natural small-molecules based on the combinational use of biolayer interferometry and UHPLC-DAD-Q/TOF-MS/MS, Acta Pharm. Sin. B 12 (2022) 1723-1739. https://doi.org/10.1016/j.apsb.2021.08.030.

[8] X. Zhou, J. Wang, L. Yu, et al., Mitophagy and cGAS-STING crosstalk in neuroinflammation, Acta Pharm. Sin. B 14 (2024) 3327-3362. https://doi.org/https://doi.org/10.1016/j.apsb.2024.05.012.

[9] F. Ren, J. Wei, Q. Chen, et al., Artificial intelligence-driven multi-omics approaches in Alzheimer's disease: progress, challenges, and future directions, Acta Pharm. Sin. B 15 (2025) 4327-4385. https://doi.org/10.1016/j.apsb.2025.07.030.

[10] P. Scheltens, B. de Strooper, M. Kivipelto, et al., Alzheimer's disease, Lancet 397 (2021) 1577-1590. https://doi.org/10.1016/s0140-6736(20)32205-4.

[11] S. Li, Y. Wei, Z. Liang, et al., Review on dietary supplements as an effective improvement of Alzheimer's disease: focus on structures and mechanisms, Food Sci. Hum. Wellness 13 (2024) 1787-1805. https://doi.org/10.26599/FSHW.2022.9250150.

[12] J. Zhou, M. Tang, W. Li, et al., Diet and physical activity influence the composition of gut microbiota, benefit on Alzheimer's disease, Food Sci. Hum. Wellness 13 (2024) 541-555. https://doi.org/10.26599/FSHW.2022.9250049.

[13] Y. Zhang, H. Chen, R. Li, et al., Amyloid β-based therapy for Alzheimer's disease: challenges, successes and future, Signal Transduct. Target. Ther. 8 (2023) 248. https://doi.org/10.1038/s41392-023-01484-7.

[14] V. Calsolaro, P. Edison, Neuroinflammation in Alzheimer's disease: current evidence and future directions, Alzheimers Dement. 12 (2016) 719-732. https://doi.org/10.1016/j.jalz.2016.02.010.

[15] S. Chen, Q. Zhou, Y. Ni, et al., Autophagy and Alzheimer's disease, Adv. Exp. Med. Biol. 1207 (2020) 3-19. https://doi.org/10.1007/978-981-15-4272-5_1.

[16] T. Liang, Y. Zhang, S. Wu, et al., The role of NLRP3 inflammasome in Alzheimer's disease and potential therapeutic targets, Front. Pharmacol. 13 (2022) 845185. https://doi.org/10.3389/fphar.2022.845185.

[17] A.G. Wu, X.G. Zhou, G. Qiao, et al., Targeting microglial autophagic

degradation in NLRP3 inflammasome-mediated neurodegenerative diseases, Ageing Res. Rev. 65 (2021) 101202. https://doi.org/10.1016/j.arr.2020.101202.

[18] M. Sharma, E. de Alba, Structure, activation and regulation of NLRP3 and AIM2 inflammasomes, Int. J. Mol. Sci. 22 (2021) 872. https://doi.org/10.3390/ijms22020872.

[19] N. Kelley, D. Jeltema, Y. Duan, et al., The NLRP3 inflammasome: an overview of mechanisms of activation and regulation, Int. J. Mol. Sci. 20 (2019) 3328. https://doi.org/10.3390/ijms20133328.

[20] Q. Ma, Pharmacological inhibition of the NLRP3 inflammasome: structure, molecular activation, and inhibitor-NLRP3 interaction, Pharmacol. Rev. 75 (2023) 487-520. https://doi.org/10.1124/pharmrev.122.000629.

[21] Z. Zhong, S. Liang, E. Sanchez-Lopez, et al., New mitochondrial DNA synthesis enables NLRP3 inflammasome activation, Nature 560 (2018) 198-203. https://doi.org/10.1038/s41586-018-0372-z.

[22] Y.S. Feng, Z.X. Tan, L.Y. Wu, et al., The involvement of NLRP3 inflammasome in the treatment of Alzheimer's disease, Ageing Res. Rev. 64 (2020) 101192. https://doi.org/10.1016/j.arr.2020.101192.

[23] J. Fu, H. Wu, Structural mechanisms of NLRP3 inflammasome assembly and activation, Annu. Rev. Immunol. 41 (2023) 301-316. https://doi.org/10.1146/annurev-immunol-081022-021207.

[24] J. Kim, H.J. Lee, S.K. Park, et al., Donepezil regulates LPS and Aβ-stimulated neuroinflammation through MAPK/NLRP3 inflammasome/STAT3 signaling, Int. J. Mol. Sci. 22 (2021) 10637. https://doi.org/10.3390/ijms221910637.

[25] A. Nakanishi, N. Kaneko, H. Takeda, et al., Amyloid β directly interacts with NLRP3 to initiate inflammasome activation: identification of an intrinsic NLRP3 ligand in a cell-free system, Inflamm. Regen. 38 (2018) 27. https://doi.org/10.1186/s41232-018-0085-6.

[26] M. Guo, Z. Wang, X. Zhou, et al., Ciliatoside A attenuates neuroinflammation in Alzheimer's disease by activating mitophagy and inhibiting NLRP3 inflammasome activation, Phytomedicine 145 (2025) 156928. https://doi.org/10.1016/j.phymed.2025.156928.

[27] D. Glick, S. Barth, K.F. Macleod, Autophagy: cellular and molecular mechanisms, J. Pathol. 221 (2010) 3-12. https://doi.org/10.1002/path.2697.

[28] D.J. Klionsky, G. Petroni, R.K. Amaravadi, et al., Autophagy in major human diseases, EMBO J. 40 (2021) e108863. https://doi.org/10.15252/embj.2021108863.

[29] A.G. Wu, R. Pan, B.Y. Law, et al., Targeting autophagy as a therapeutic strategy for identification of liganans from *Peristrophe japonica* in Parkinson's disease, Signal Transduct. Target. Ther. 6 (2021) 67. https://doi.org/10.1038/s41392-020-00442-x.

[30] W.Q. Qiu, W. Ai, F.D. Zhu, et al., Polygala saponins inhibit NLRP3 inflammasome-mediated neuroinflammation via SHP-2-Mediated mitophagy, Free Radic. Biol. Med. 179 (2022) 76-94. https://doi.org/10.1016/j.freeradbiomed.2021.12.263.

[31] X.G. Zhou, W.Q. Qiu, L. Yu, et al., Targeting microglial autophagic degradation of the NLRP3 inflammasome for identification of thonningianin A in Alzheimer's disease, Inflamm. Regen. 42 (2022) 25. https://doi.org/10.1186/s41232-022-00209-7.

[32] Q. Liang, H.H. Gou, L.P. Chen, et al., "Food & medicine homology" medicines and their formulas: a versatile approach for the management of lipid metabolic disorders related diseases, Food Med. Homol. 3 (2026) 9420130. https://doi.org/10.26599/FMH.2026.9420130.

[33] C. Esposito, C. Santarcangelo, R. Masselli, et al., *Epilobium angustifolium* L. extract with high content in oenothein B on benign prostatic hyperplasia: a monocentric, randomized, double-blind, placebo-controlled clinical trial, Biomed. Pharmacother. 138 (2021) 111414. https://doi.org/10.1016/j.biopha.2021.111414.

[34] X. Han, T. Xu, Q. Fang, et al., Quercetin hinders microglial activation to alleviate neurotoxicity via the interplay between NLRP3 inflammasome and mitophagy, Redox Biol. 44 (2021) 102010. https://doi.org/10.1016/j.redox.2021.102010.

[35] H. Zhang, Z. Zhang, S. Wang, et al., Apoptotic induction of mitochondria-anchored aggregation-induced emission luminogens through the intrinsic mitochondrial pathway, ACS Omega 7 (2022) 47912-47922. https://doi.org/10.1021/acsomega.2c05761.

[36] P. Prakash, K.P. Jethava, N. Korte, et al., Monitoring phagocytic uptake of amyloid β into glial cell lysosomes in real time, Chem. Sci. 12 (2021) 10901-10918. https://doi.org/10.1039/d1sc03486c.

[37] A. Reifschneider, S. Robinson, B. van Lengerich, et al., Loss of TREM2 rescues hyperactivation of microglia, but not lysosomal deficits and neurotoxicity in models of progranulin deficiency, EMBO J. 41 (2022) e109108. https://doi.org/10.15252/embj.2021109108.

[38] F.D. Zhu, X. Chen, L. Yu, et al., Targeting autophagy to discover the *Piper wallichii* petroleum ether fraction exhibiting antiaging and anti-Alzheimer's disease effects in *Caenorhabditis elegans*, Phytomedicine 117 (2023) 154916. https://doi.org/10.1016/j.phymed.2023.154916.

[39] F.D. Zhu, B.D. Wang, D.L. Qin, et al., *Carpesii fructus* extract exhibits neuroprotective effects in cellular and *Caenorhabditis elegans* models of Parkinson's disease, CNS Neurosci. Ther. 30 (2024) e14515. https://doi.org/10.1111/cns.14515.

[40] C.G. Zou, Y.C. Ma, L.L. Dai, et al., Autophagy protects *C. elegans* against necrosis during *Pseudomonas aeruginosa* infection, Proc. Natl. Acad. Sci. 111 (2014) 12480-12485. https://doi.org/10.1073/pnas.1405032111.

[41] Q. Zhang, M. Zeng, B. Zhang, et al., Evening primrose and its compounds of 1-oxohederagenin and remangilone C ameliorate bleomycin-induced pulmonary fibrosis by regulating *β*-catenin signaling, Phytomedicine 133 (2024) 155933. https://doi.org/10.1016/j.phymed.2024.155933.

[42] S. Moonen, M.J. Koper, E. van Schoor, et al., Pyroptosis in Alzheimer's disease: cell type-specific activation in microglia, astrocytes and neurons, Acta. Neuropathol. 145 (2023) 175-195. https://doi.org/10.1007/s00401-022-02528-y.

[43] J. Sun, X. Huang, X. Han, et al., Tetrahydroxy stilbene glucoside alleviates ADHD related symptoms by improving neuroinflammation and BDNF signaling pathway: bioinformatic analysis and experimental verification, Clin. Tandit. Med. Pharmacol. 6 (2025) 200218. https://doi.org/10.1016/j.ctmp.2025.200218.

[44] M. Biasizzo, N. Kopitar-Jerala, Interplay between NLRP3 inflammasome and autophagy, Front. Immunol. 11 (2020) 591803. https://doi.org/10.3389/fimmu.2020.591803.

[45] D.A. Dias, S. Urban, U. Roessner, A historical overview of natural products in drug discovery, Metabolites 2 (2012) 303-336. https://doi.org/10.3390/metabo2020303.

[46] L. Deng, C. Yin, X. Zhou, et al., Targeted degradation of aberrant tau for the discovery of Pulsatilla chinensis in Alzheimer's disease, Chin. Med. 21 (2026) 137. https://doi.org/10.1186/s13020-025-01276-x.

[47] L. Yan, M.S. Guo, Y. Zhang, et al., Dietary plant polyphenols as the potential drugs in neurodegenerative diseases: current evidence, advances, and opportunities, Oxid. Med. Cell Longev. 2022 (2022) 5288698. https://doi.org/10.1155/2022/5288698.

[48] K. Cadwell, Crosstalk between autophagy and inflammatory signalling pathways: balancing defence and homeostasis, Nat. Rev. Immunol. 16 (2016) 661-675. https://doi.org/10.1038/nri.2016.100.

[49] Z. Zhong, E. Sanchez-Lopez, M. Karin, Autophagy, NLRP3 inflammasome and auto-inflammatory/immune diseases, Clin. Exp. Rheumatol. 34 (2016) 12-16.

[50] J. Houtman, K. Freitag, N. Gimber, et al., Beclin1-driven autophagy modulates the inflammatory response of microglia via NLRP3, EMBO J. 38 (2019) EMBJ201899430. https://doi.org/10.15252/embj.201899430.

[51] Y.Y. Yong, L. Zhang, Y.J. Hu, et al., Targeting autophagy regulation in NLRP3 inflammasome-mediated lung inflammation in COVID-19, Clin. Immunol. 244 (2022) 109093. https://doi.org/10.1016/j.clim.2022.109093.

[52] M.S. Uddin, A. Stachowiak, A.A. Mamun, et al., Autophagy and Alzheimer's disease: from molecular mechanisms to therapeutic implications, Front. Aging Neurosci. 10 (2018) 4. https://doi.org/10.3389/fnagi.2018.00004.